

## Quantitative Morphology of Galaxies in the Hubble Deep Field

Francine R. Marleau

Department of Astronomy, University of California, Berkeley,  
Campbell Hall, Berkeley, CA 94720, USA

and

Luc Simard

UCO/Lick Observatory, University of California, Santa Cruz, CA 95064, USA

### ABSTRACT

We measure quantitative structural parameters of galaxies in the Hubble Deep Field (HDF) on the drizzled F814W images. Our structural parameters are based on a two-component surface brightness made up of a Sérsic profile and an exponential profile. We compare our results to the visual classification of van den Bergh *et al.* (1996) and the  $C - A$  classification of Abraham *et al.* (1996a). Our morphological analysis of the galaxies in the HDF indicates that the spheroidal galaxies, defined here as galaxies with a dominant bulge profile, make up for only a small fraction, namely 8% of the galaxy population down to  $m_{F814W}(AB) = 26.0$ . We show that the larger fraction of early-type systems in the van den Bergh sample is primarily due to the difference in classification of 40% of small round galaxies with half-light radii  $< 0''.31$ . Although these objects are visually classified as elliptical galaxies, we find that they are disk-dominated with bulge fractions  $< 0.5$ . Given the existing large dataset of HDF galaxies with measured spectroscopic redshifts, we are able to determine that the majority of distant galaxies ( $z > 2$ ) from this sample are disk-dominated. Our analysis reveals a subset of HDF galaxies which have profiles flatter than a pure exponential profile.

*Subject headings:* galaxies: evolution — galaxies: formation — galaxies: fundamental parameters

## 1. Introduction

Starting from our knowledge of gravity and the effects of local gravitational instabilities on the evolution of the Universe, we can infer scenarios for galaxy formation that predict the current state of the Universe. The evolutionary path followed by these perturbations as they develop to become present-day galaxies is poorly constrained. It depends on the star formation history of galaxies and the initial conditions of the gravitational collapse (Steinmetz & Müller 1995), and both are not directly observable. However, the structure and kinematics of galaxies, which are tied to their formation process (Okamura *et al.* 1988), are quantities that can be measured from observations. The structural parameters (shape, size, axial ratios, etc.) of large samples of distant galaxies play therefore an important if not unique role in the multi-parameter study that is inevitably required to understand and explain the origin of galaxies.

The properties of the galaxy population over the redshift range  $0 < z < 1$  have been studied extensively from faint redshift surveys (Lilly *et al.* 1996; Cowie *et al.* 1996; Ellis *et al.* 1996). These surveys have shown that the galaxy population is evolving in number density and/or luminosity and that this evolution depends strongly on color. However, galaxy number counts and redshifts are insufficient to determine which part of the galaxy population is evolving and how. In order to understand the role of each galaxy type in the evolution seen at intermediate redshift, morphological information must be extracted for field galaxies using an objective classification method. For the nearby sample, the existing morphological classification is based solely on visual inspection of galaxy *B*-band images, a method introduced with the work of Hubble (1926, 1930) and developed by de Vaucouleurs (1959) and Sandage (1961). The surface brightness profile of galaxies can in fact be quantified using empirical luminosity laws such as the  $r^{1/4}$  law associated with the spheroidal populations (de Vaucouleurs 1948, 1953) and the exponential profile describing the disks of galaxies (Patterson 1940; de Vaucouleurs 1956). These profiles exist for a restricted number of nearby field and cluster galaxies and have not been used until recently, with the development of photometric decomposition methods (Schade *et al.* 1996; Abraham *et al.* 1996b), to classify distant galaxies in a consistent way.

Visual classification is increasingly difficult for faint or high redshift galaxies, or both, and it is therefore necessary to use a quantitative profile decomposition method to retrieve the physical properties of the observed two-dimensional (2D) images of galaxies. When comparing nearby galaxy samples with high redshift galaxies, it is also essential to establish a correspondence between visual and quantitative classifications. Quantitative classification has two major advantages over visual classification: (1) it is reproducible, and (2) biases can be understood and carefully characterized through simulations which are treated as real data. The detailed images of the Hubble Deep Field (HDF) provide an ideal dataset of nearby and distant field galaxies for the study of morphological properties of galaxies in the context of evolution. The HDF is a Hubble Space Telescope (HST) program that has imaged a field in the northern continuous viewing zone for ten consecutive days, or approximately 150 orbits, in four passbands (Williams *et al.* 1996). The morphologies of HDF galaxies in the range  $21 < I < 25$  have been visually classified (van den Bergh *et al.* 1996, hereafter VDB96) and measured using a quantitative classification system based on the study of the central concentration and asymmetry of the galaxian light (Abraham *et al.* 1996a, hereafter ABR96). These classification techniques find that the fraction of elliptical galaxies in the HDF is as large as 30% (although the classification by ABR96 gives a value closer to 20%), with the remainder being divided into 31% spirals and 39% unclassified.

In this paper, we examine the structural properties of the galaxies in the HDF using a new 2D photometric decomposition fitting algorithm. We present the structural parameter distributions of HDF

galaxies and compare our results to previous classification schemes. The outline of this paper is as follows: Section 2 describes the photometric decomposition method that we use to determine morphological properties of the HDF galaxies. In this section, we also present the results of simulations that test the ability of our method to measure reliably galaxian structural parameters. In Section 3 we present the results of our photometric decomposition technique applied to the HDF. Section 4 considers previous classification schemes of HDF galaxies and underlines the differences between classification methods. Section 5 deals with the limitations of the standard bulge/disk decomposition model and the observed deviations from that model for a number of galaxies in the HDF. We summarize our conclusions and discuss their implications for galaxy evolution in Section 6.

## 2. Two-Dimensional Modeling of Galaxy Images

### 2.1. Photometry

We used the SExtractor galaxy photometry package version 1.0a (Bertin & Arnouts 1996) on the publicly released version 2 drizzled  $F814W$  images of the HDF with a detection threshold of  $1.5\sigma$  and a minimum object area of 30 pixels. The total sky area analyzed was  $16085 \text{ arcsec}^2$ . The resulting SExtractor catalogs contained 566 objects from WFPC2-chip 2, 498 objects from chip 3 and 575 objects from chip 4 for a total of 1639 objects. As SExtractor performs galaxy photometry, it constructs a “segmentation” image. Pixels belonging to the same object all have the same values in this segmentation image. It can therefore be used as a pixel mask for the surface brightness profile fits. SExtractor deblends objects using multiple flux thresholding. At each flux threshold, it computes the number of possible independent “branches”, and the fraction of the total flux contained in each one. The SExtractor deblending parameter *DEBLEND\_MINCONT* sets the minimum fraction of the total flux a branch must contain to be considered as a separate object. We used a *DEBLEND\_MINCONT* value of 0.001 as our definition of a distinct object. As shown in Section 3.2, our galaxy number counts are identical to those of previous investigators (e.g. Bouwens *et al.* 1997).

For each object, we used the following SExtractor parameters: centroid  $X$  and  $Y$ , local sky background level and variance and the  $1.5\sigma$  isophotal area. We extracted an area around each object 20 times larger than its isophotal area from both the science image and the segmentation image to ensure that our fitting routine would successfully discriminate between galaxy and sky fluxes.

### 2.2. Surface Brightness Profile Model

The structure of each detected galaxy in the HDF was examined carefully using GIM2D (Galaxy Image 2D), a 2D decomposition fitting program (Simard 1998). GIM2D is an IRAF/SPP package written to perform detailed surface brightness profile decompositions of low signal-to-noise (S/N) images of distant galaxies in a fully automated way. GIM2D takes an input image, does a 2D profile fit on the image pixels belonging to the same pixel value segmentation image, and produces a galaxy-subtracted image as well as a catalog of structural parameters. The 2D galaxy model used by GIM2D has a maximum of twelve parameters: the total flux  $F$  in data units (DU), the bulge fraction  $B/T$  ( $0$ =pure disk system), the bulge effective radius  $r_e$ , the bulge ellipticity  $e$  ( $e \equiv 1 - b/a$ ,  $b \equiv$  semi-minor axis,  $a \equiv$  semi-major axis), the bulge position angle of the major axis  $\phi_b$  (clockwise,  $0$ =y-axis), the exponential disk scale length  $r_d$ , the disk inclination  $i$  ( $0$ =face-on), the disk position angle  $\phi_d$ , the subpixel  $dx$  and  $dy$  offsets of the galaxy center, the

background level  $b$ , and the Sérsic index  $n$ . One or more parameters can be frozen to some initial values if necessary. We did not constrain  $\phi_b$  and  $\phi_d$  to be equal for two reasons: (1) a large difference between these position angles is a signature of barred spirals, and (2) we have observed galaxies with *bona fide* bulges which were not quite aligned with the disk position angle. All total fluxes  $F$  were converted in this paper to  $F_{814W}$  magnitudes on the AB system using the equation:

$$m_{F814W}(AB) = -2.5\log_{10}(F/t) + C, \quad (1)$$

where  $C = 22.09$  for WF2, 22.09 for WF3, and 22.07 for WF4. The total exposure time  $t$  was 123600 seconds in the  $F814W$  filter (Williams *et al.* 1996).

The first component (“bulge”) of the 2D surface brightness used by GIM2D to model galaxy images is a Sérsic (1968) profile of the form:

$$\Sigma(r) = \Sigma_e \exp\{-b[(r/r_e)^{1/n} - 1]\}, \quad (2)$$

where  $\Sigma(r)$  is the surface brightness at radius  $r$ . The parameter  $b$  is set equal to  $1.9992n - 0.3271$  so that  $r_e$  remains the projected radius enclosing half of the light in this component (Capaccioli 1989). The classical de Vaucouleurs profile therefore has the special value  $n = 4$ . The second component (“disk”) is a simple exponential profile of the form:

$$\Sigma(r) = \Sigma_0 \exp(-r/r_d). \quad (3)$$

$\Sigma_0$  is the central surface brightness. We adopted here the conventional “bulge/disk” nomenclature and assumed this distinction in the galaxies light profile classification throughout this paper. Nevertheless, it should be kept in mind that this nomenclature does not say anything about the internal kinematics of the components. The presence of a “disk” component does not imply the presence of an actual disk since many virially-supported systems also have simple exponential profiles.

The WFPC2 detector undersampling was taken into account by generating the surface brightness model on an oversampled grid, convolving it with the appropriate point spread function (PSF), shifting its center according to  $dx$  and  $dy$  and rebinning the result to the detector resolution for direct comparison with the observed galaxy image. The PSF was generated by the Space Telescope package *TINY TIM* (Krist 1993) and subsampled to reproduce the pixel resolution of the HDF. As a first pass for our morphological analysis, we fitted all the objects in our HDF catalog as the sum of a de Vaucouleurs profile and a simple exponential. However, as discussed in Section 5, we discovered that this model failed for a number of galaxies which had surface brightness profiles *flatter* than a *pure* ( $B/T = 0$ ) exponential profile. The second pass in our morphological analysis therefore consisted of fitting *pure* Sérsic profiles to these galaxies with a Sérsic index  $n$  allowed to vary between 0.2 and 4.0.

### 2.3. Fitting Algorithm

The 12-dimensional parameter space can have a very complicated topology with local minima at low S/N ratios. It was therefore important to choose an algorithm which did not easily get fooled by those local minima. The Metropolis algorithm (Metropolis *et al.* 1953, Saha & Williams 1994) was designed to search for optimal parameter values in a complicated topology. Compared to gradient search methods, the Metropolis is not efficient i.e. it is CPU intensive. On the other hand, gradient searches are lazy. They will start from initial parameter values, dive in the first minimum they encounter and claim it is the global one.

The Metropolis algorithm in GIM2D starts from an initial set of parameters given by the image moments of the object and computes the likelihood  $P(w|D, M)$  that the parameter set  $w$  is the true one given the data  $D$  and the model  $M$ . It then generates random perturbations  $\Delta \mathbf{x}$  about that initial location with a given “temperature”. When the search is “hot”, large perturbations are tried. After each trial perturbation, the Metropolis algorithm computes the likelihood value  $P_1$  at the new location, and immediately accepts the trial perturbation if  $P_1$  is greater than the old value  $P_0$ . However, if  $P_1 < P_0$ , then the Metropolis algorithm will accept the trial perturbation only  $P_1/P_0$  of the time. Therefore, the Metropolis algorithm will sometime accept trial perturbations which take it to regions of lower likelihood. This apparently strange behavior is very valuable: if the Metropolis algorithm finds a minimum, it will try to get out of it, but it will only have a finite probability (related to the depth of the minimum) of succeeding. The “temperature” is regulated according to the number of accepted iterations. If the Metropolis accepts too many trial perturbations, then the search is too “cold”, and the temperature must be increased. Conversely, if the Metropolis rejects too many trial perturbations, then the search is too “hot”, and the temperature must be decreased. The Metropolis temperature is regulated such that half of the trial perturbations are accepted. The more commonly known simulated annealing technique is a variant and a special case of the Metropolis algorithm in which the temperature is only allowed to decrease until the “ground-state” is reached.

The step matrix for the trial perturbations  $\Delta \mathbf{x}$  is given by the simple equation  $\Delta \mathbf{x} = Q \cdot \vec{u}$  where the vector  $\vec{u}$  consists of randomly generated numbers between 0 and 1, and the matrix  $Q$  is obtained through Choleski inversion of the local covariance matrix of accepted iterations (Vanderbilt & Louie 1984). In short, the sampling of parameter space shapes itself to the local topology.

Convergence is achieved when the difference between two likelihood values separated by 100 iterations is less than  $3\sigma$  of the likelihood fluctuations. After convergence, the Metropolis algorithm Monte-Carlo samples the region where the likelihood is thus maximized and stores the accepted parameter sets as it goes along to build the distribution  $P(w|D, M)$ . Once the region has been sufficiently sampled, the Metropolis algorithm computes the median of  $P(w|D, M)$  for each model parameter as well as the 99% confidence limits. The output of the fitting process consists of a PSF-convolved model image  $O$ , a residual image  $R$ , and a log file containing all Metropolis algorithm iterations, the final parameter values and their confidence intervals.

## 2.4. Asymmetry Index

The residuals from the smooth model fits were analyzed to give further information on the morphology of the galaxies. The nature of asymmetric residuals is of particular interest to galaxy evolution. For example, the presence of star-forming regions or a recent merger event generally give rise to asymmetric features. An asymmetry index was extracted from the residual image to assess the nature of the non-smooth 2D profiles. For each object analyzed by GIM2D, a reduced chi-square  $\chi_R^2$ , a measure of the residual flux, and a seeing-deconvolved half-light radius  $r_{hl}$  were obtained. The half-light radius was computed by integrating equations 2 and 3 with the measured structural parameters. The parameter  $R_A$  was calculated using the following expression:

$$R_A = \frac{\frac{1}{2} \sum |R_{ij} - R_{ij}^{180}|}{\sum I_{ij}}, \quad (4)$$

where  $I_{ij}$ ,  $R_{ij}$  and  $R_{ij}^{180}$  are the flux at  $(i, j)$  in the input original image, the residual image, and the residual image rotated by 180 degrees, respectively. Aperture sizes ranging from 1–10  $r_{hl}$  were used. The index

$R_A$  is calculated over the same pixels used in the bulge/disk fits. This parameter is equivalent to the asymmetric residual flux index defined in Schade *et al.* (1995) when computed within a radius of  $5 h_{50}^{-1}$  kpc. Background noise absolute pixel values in equation 4 can make significant contributions to  $R_A$  even in the absence of any residual. This background contribution was removed by computing a correction for  $R_A$  over a sky background area equal to the object area and subtracting the result from the “raw”  $R_A$  values. The background corrected  $R_A$  converged to constant values at large radii.

### 3. Results of the Photometric Decompositions

#### 3.1. The HDF Catalog

Profile fitting was done for a total of 1639 objects in the HDF. For each galaxy, we obtained a PSF-convolved model image, a residual image, the best parameter values with their confidence limits, and the reduced chi-square  $\chi_R^2$ . Figure 1 shows a section of the WFPC2-chip 4 HDF image and the residual image created by GIM2D after detailed photometric decompositions have been performed on all galaxies in the field.

In Table 1 we present the best structural parameter values with their confidence limits and the goodness of the fit for the 522 galaxies with  $m_{F814W} \leq 26.0$  in the HDF analyzed with GIM2D. The Sérsic parameters for the subsample of HDF galaxies discussed in Section 5 are given in Table 2. Only the WFPC2-chip 4 sample of these extensive tabulations of data are printed here and the complete tables are stored in the electronic archive of The Astrophysical Journal, from which they can be retrieved with the standard procedure (also available at <http://astro.berkeley.edu/~marleau/>).

#### 3.2. Bulge and Disk Structural Parameter Distributions

The HDF is the deepest field ever imaged with the superior angular resolution of HST. Consequently, the structural parameter distributions of HDF galaxies provide unique tests of galaxy evolution models (Bouwens *et al.* 1997). This section focuses on the *observed* and *intrinsic* structural parameter distributions of HDF galaxies. Intrinsic distributions fully take selection effects into account and should be compared with theoretical predictions.

The *observed* distributions of structural parameters for our entire sample of 1639 galaxies are shown in Figure 2. Bulge parameter distributions ( $r_e$ ,  $e$ ,  $\phi_b$ ) only include objects with  $B/T > 0.5$  whereas disk parameter distributions ( $r_d$ ,  $i$ ,  $\phi_d$ ) only include objects with  $B/T \leq 0.5$ . Such a separation is needed to minimize the scatter in those distributions caused by poorly constrained bulge parameters in disk-dominated galaxies and vice versa. Figure 3 shows the same distributions for galaxies brighter than  $m_{F814W}(AB) = 26.0$ . The distributions of half-light radii for different  $m_{F814W}(AB)$  cuts are shown in Figure 4. The half-light radius versus  $B/T$  distribution in Figure 4 suggests that there are no large ellipticals in our HDF sample.

The observed parameter distributions of galaxies must be corrected for the galaxy selection function of the SExtractor detection algorithm to produce the final intrinsic parameter distributions. The detection thresholding method used by SExtractor depends critically on galaxy apparent surface brightness. The probability that a given object will be detected depends on total flux  $F$ , bulge fraction  $B/T$ , bulge effective radius  $r_e$ , bulge ellipticity  $e$ , disk scale length  $r_d$ , and disk inclination  $i$ . For example, objects with larger

$B/T$  will be easier to detect because they are more concentrated, and large objects will be harder to detect than smaller ones at a fixed total flux. In order to derive true intrinsic structural parameter distributions, we must therefore construct a six-dimensional galaxy selection function  $S(\omega)$  over all parameter space locations  $\omega \equiv (F, B/T, r_e, e, r_d, i)$  and use it to “flat-field” the observed structural parameter distributions. The selection function does not depend on the bulge and disk position angles.

We built  $S(\omega)$  by generating 66000 galaxies that were modeled with structural parameter values uniformly covering the structural parameter ranges:  $23.2 \leq m_{F814W}(AB) \leq 29.0$ ,  $0 \leq B/T \leq 1$ ,  $0 \leq r_e \leq 0''.8$ ,  $0 \leq e \leq 0.7$ ,  $0 \leq r_d \leq 0''.8$ ,  $0 \leq i \leq 85^\circ$ . Each model galaxy was added one at a time to an empty section of the HDF covering  $6''.0 \times 5''.2$ . “Empty” here means that no objects were detected by SExtractor in that sky section with the same detection parameters used to construct our object catalog. Using an empty section of the HDF ensured that we were building  $S(\omega)$  with the real background noise that was “seen” by the detection algorithm. The background “noise” included read-out, sky and the brightness fluctuations of all the very faint galaxies that were beyond our detection threshold. This last contribution to the background noise is particularly hard to model theoretically, and our approach bypassed this problem. We divided parameter space into 320 “cells” with the number of cells along each dimensions being  $(N_m, N_{B/T}, N_{r_e}, N_e, N_{r_d}, N_i, N_{r_{hl}}) = (8, 5, 1, 1, 1, 1, 8)$ . SExtractor was run on all 66000 images to determine the number of detected models  $D(\omega)$  in each cell. The selection function  $S(\omega)$  (shown in Figure 5) was simply  $D(\omega)$  divided by the number of models  $G(\omega)$  generated in that cell in parameter space.  $S(\omega)$  was set automatically to one for cells with  $m_{F814W}(AB) \leq 23.2$ . One-dimensional distributions for  $m_{F814W}(AB)$ ,  $B/T$ , and  $r_{hl}$  were created by integrating over all cells with  $S(\omega)$  greater than or equal to a fixed limit  $S_{lim}$ .

Even though measured structural parameters were not reliable fainter than  $m_{F814W}(AB) = 26.0$ , the observed and intrinsic distributions of  $m_{F814W}(AB)$ ,  $B/T$ , and  $r_{hl}$  over the magnitude range  $21.0 \leq m_{F814W}(AB) \leq 29.0$  (Figure 6) were first calculated to provide an “upper limit” on the intrinsic parameter distributions. The top and bottom distributions are for  $S_{lim} \geq 0.1$  and  $S_{lim} \geq 0.5$ . Figure 7 displays the same distributions as Figure 6 for  $21.0 \leq m_{F814W}(AB) \leq 26.0$ . Except for the case where  $21.0 \leq m_{F814W}(AB) \leq 29.0$  and  $S_{lim} = 0.1$ , the selection function corrections are relatively small. It is worth noting that all  $B/T$  intrinsic distributions show that the detection algorithm is biased against pure disk systems (see the  $21.0 \leq m_{F814W}(AB) \leq 26.0$  distributions for example) as expected since pure disk systems are less centrally concentrated than  $r^{1/4}$  profiles and thus harder to detect. So, the intrinsic ratio of the number of disk-dominated systems to the number of bulge-dominated is likely to be higher than the observed one.

### 3.3. Asymmetry Parameter Distribution

The deviation from smoothness and symmetry are striking features of the morphologies of HDF galaxy images. Some fraction of the galaxies in the HDF contain profile irregularities which may significantly perturb fits of elliptically symmetric two-dimensional models. These irregularities have two causes: (1) the morphologies of high redshift spiral and starburst galaxies change radically as the observed bandpass shifts to the rest-frame UV where HII regions dominate the galaxy light distribution (Giavalisco *et al.* 1996a), and (2) some galaxies are just intrinsically more disturbed. We analyzed the residuals of our galaxy sample with  $m_{F814W}(AB) \leq 26.0$  by evaluating the asymmetry index given in Section 2.4. The results are presented in Figure 8 for  $R_A$  computed within a  $2r_{hl}$  aperture. Also shown in Figure 8 is a measure of the residual flux  $\chi_R^2$  as a function of the degree of asymmetry  $R_A$  for our sample of galaxies. The index  $R_A$  remains smaller than  $\sim 20\%$  for the majority of galaxies (those objects with  $R_A > 0.3$  are positioned near

the edge of the chip where it is most difficult to evaluate the sky background correction accurately).

Non-smooth local features in a galaxy 2D light profile can alter the best parameters derived with GIM2D depending on their brightnesses and positions in the galaxy. For example, a very bright feature at the center of the galaxy will cause the bulge component to be overestimated. We measured the effects of clumps or asymmetric features on the extracted smooth 2D profile parameters through simulations. An asymmetric light component, in the form of one or multiple “blobs”, i.e. unresolved sources convolved with the PSF, was added to the simulated smooth 2D profile image. The input parameters for generating the asymmetric features are the number of blobs  $n_b$ , the fraction of total galaxy flux in the blobs  $F_b$ , and the blobs’ maximum galactocentric distance  $r_b$ . The positions and fluxes of the blobs were randomly generated within the limits imposed by  $F_b$  and  $r_b$ .

Asymmetric features superposed on the smooth profile were generated randomly for  $n_b = 5$  and  $r_b = 1.5r_{hl}$ . We tested five discrete flux levels ( $F_b = 0.0, 0.05, 0.10, 0.15, 0.20$ ) in order to sample the same range of residual fluxes as seen in the real data (see Figure 8). For each given  $F_b$ , we generated 10 galaxies with the following structural parameters:  $m_{F814W}(AB) = 24.0$ ,  $B/T = 0.3$ ,  $r_e = 0.''12$ ,  $e = 0.2$ ,  $r_d = 0.''32$ ,  $i = 20^\circ$ ,  $\phi_b = \phi_d = 60^\circ$ , and  $n = 4.0$ . The 50 simulated asymmetric galaxy images were analyzed exactly the same way as the real data. The detections were classified by SExtractor as “single” or “multiple”. The average number of detections in a single simulated galaxy image increased with  $F_b$  as expected. As for the real data, profile fitting was done on the simulated image pixels belonging to the same pixel value segmentation image. An example of a simulated image with a flux fraction  $F_b = 0.10$  is shown in Figure 9. For each  $F_b$ , we were able to examine the parameters recovered by GIM2D. The recovery success for the bulge fraction parameter are displayed in Figure 9. The mean of the measured  $B/T$  going from  $F_b = 0.0$  to  $F_b = 0.20$  are 0.299 ( $\sigma=0.016$ ), 0.270 (0.084), 0.253 (0.080), 0.282 (0.161), and 0.411 (0.218) with a total number of galaxies per bin of 10. The simulations showed that the perturbations to the profiles caused by the presence of asymmetric features did not systematically and significantly alter the measured bulge fraction over the range of galaxy asymmetric residual fluxes seen in the data. The RMS (root-mean-square), which increased with  $F_b$ , ranged from 1-20%, and the mean remained close to the input value of  $B/T = 0.3$ . Therefore, we do not expect the non-smooth galaxy features to change the total distribution of  $B/T$  we derived from our galaxy sample in Section 3.2.

### 3.4. Structural Parameter Recovery Simulations

The results of this paper discussed below in Sections 4 and 5 rely on our ability to measure (1) accurate structural bulge/disk parameters for small galaxies and (2) the index  $n$  of pure Sérsic profiles over the range  $0.2 \leq n \leq 4$ . We tested the reliability of our structural parameters through simulations. We created 600 galaxies with structural parameters uniformly generated at random in the following ranges:  $m_{F814W}(AB) \geq 24.4$ ,  $0.0 \leq B/T \leq 1.0$ ,  $0 \leq r_e \leq 0.''3$ ,  $0 \leq e \leq 0.7$ ,  $0 \leq r_d \leq 0.''3$ ,  $0 \leq i \leq 85^\circ$ , and  $0.2 \leq n \leq 4.0$ . The  $r_e$  and  $r_d$  ranges cover the bulk of the real HDF galaxy size distributions (see Section 3.2). We did not impose any correlation between structural parameters. Sky subtraction errors can lead to substantial errors on structural parameter estimates especially for steep profiles such as the  $r^{1/4}$  law profile. Indeed, the half-light radius of a bulge-dominated system can be underestimated if a significant fraction of the total flux is hidden in the outer wings of the profile where sky noise dominates. To characterize the effects of *real* sky subtraction errors on structural parameter estimates, we used the empty section of the HDF described in Section 3.2. Our 600 simulated bulge/disk models were added to this background image one at a time and reduced as if they were real objects.



Our simulations showed that we systematically underestimated the total magnitudes of our objects by 0.1 mag over the magnitude range  $24.4 \leq m_{F814W}(AB) \leq 26.0$  with a dispersion of 0.05 mag. The fractional total flux error quickly increased beyond 20% for objects fainter than  $m_{F814W}(AB) = 26.0$ . Our structural parameters are therefore reliable for objects brighter than  $m_{F814W}(AB) = 26.0$ . Out of the 1639 HDF objects originally analyzed with GIM2D, 522 satisfied this magnitude selection cut.

We classified HDF galaxies according to bulge fraction, and it was therefore very important to determine the reliability of our bulge fraction estimates down to our magnitude limit of  $m_{F814W}(AB) = 26.0$ . Figure 10 shows the difference between observed and input bulge fractions versus seeing-deconvolved half-light radius and  $B/T$  for three different  $B/T$  intervals ( $0 \leq B/T \leq 0.2$ ,  $0.2 < B/T \leq 0.8$ , and  $B/T > 0.8$ ) for galaxies with  $m_{F814W}(AB) \leq 26.0$ . The mean differences  $d(B/T) \equiv (B/T)_{measured} - (B/T)_{input}$  in those three bins were  $-0.00$ ,  $-0.04$  and  $-0.14$ . If we further divided our simulations into 0.1 ( $B/T$ ) bins, the mean differences going from  $B/T = 0$  to  $B/T = 1$  were  $0.003$  ( $\sigma=0.05$ ),  $-0.03$  (0.07),  $-0.04$  (0.09),  $-0.05$  (0.10),  $-0.02$  (0.17),  $-0.02$  (0.16),  $-0.04$  (0.13),  $-0.04$  (0.16),  $-0.08$  (0.13), and  $-0.19$  (0.24) with an average number of objects per bin of 45. The recovery success is lowest for  $r_{hl}$  below about 0.2 which represents only 25% of the galaxies with  $m_{F814W}(AB) \leq 26.0$ . The larger deviation in the  $B/T > 0.9$  bin has two main causes. First, we fitted a two-component model to all the objects. Our model will therefore converge to a pure bulge model only when the signal-to-noise ratio is high enough to definitely rule out the presence of a disk component. At lower signal-to-noise ratios, a disk component may be part of the model by being very small or very large. Since we did not impose any correlation between structural parameters, both extremes were present in our simulations even though they may not be in real galaxies. Second, the model can try to compensate for sky subtraction errors with a very low-surface brightness disk which would lead to an artificial decrease of the measured bulge fraction. Finally, the larger deviation in the uppermost  $B/T$  bin is also due to a smaller extent to the fact that we did not allow the  $B/T$  to exceed 1.0 in our fits. More objects will therefore be scattered out of the bin than into it.

As discussed below in Section 5, we found a number of galaxies in the HDF which could not be fitted by our model because they had surface brightness *flatter* than a pure exponential disk profile. These objects were selected based on the following two criteria: (1)  $B/T < 0.01$ , and (2) the size of the 99%  $B/T$  confidence interval had to be less than 0.01. We fitted objects satisfying both criteria using a pure Sérsic profile given by equation 2. We hereafter refer to these objects as “Sérsic” galaxies. Criterion (1) selected objects with the flattest surface brightness profiles allowed by our bulge/disk model, and criterion (2) measured the “stubbornness” of the model in its attempts to converge towards a profile flatter than a pure exponential disk. A selection based solely on criterion (1) would probably have included pure disk exponential galaxies in our sample of Sérsic galaxies. The distribution of Sérsic index values presented in Section 5 shows that none of the Sérsic galaxies we analyzed had  $n = 1$ . The combination of both criteria successfully eliminated pure disk exponential galaxies. However, criterion (2) was not ideal because the size of the confidence interval also depends on signal-to-noise: Sérsic galaxies with low S/N ratios will have larger confidence intervals even if they exhibited the same “stubbornness” to go beyond  $n = 1$  as brighter Sérsic galaxies. So, we do expect to be missing many faint Sérsic galaxies.

Our Sérsic selection criteria were tested by creating 300 simulated galaxies with pure Sérsic profiles and structural parameters in the following ranges:  $24.0 \leq m_{F814W}(AB) \leq 29.0$ ,  $r_e \leq 0''.4$ ,  $e \leq 0.7$  and  $0.2 \leq n \leq 4.0$  (recall that  $n = 4$  is a de Vaucouleurs profile, and  $n = 1$  is the classical exponential disk profile). These simulated galaxies were fitted with the combination of a de Vaucouleurs profile and a simple exponential profile. The bottom part of Figure 11 shows the measured  $B/T$  versus input  $n$  for simulations with  $24.0 \leq m_{F814W}(AB) \leq 26.0$ . For  $m_{F814W}(AB) \leq 26.0$ , 41 simulations had  $n < 1.0$ ,

but only 19 simulations passed our Sérsic selection criteria. We therefore probably identified only half of the Sérsic galaxies down to that magnitude limit in the HDF (see Section 5 for further discussion). For  $m_{F814W}(AB) \leq 24.7$ , the completeness fraction was 0.70. None of the galaxies with input  $n > 1$  met our Sérsic selection criteria.

Our study of Sérsic galaxies depends on our effectiveness to recognize them and on our ability to measure their Sérsic index  $n$  when  $n \leq 4$ . We tested our ability to successfully recover Sérsic index values by fitting pure Sérsic models to the same set of Sérsic galaxy simulations as above. The top part of Figure 11 shows the difference  $dn$  between the observed Sérsic index values and the input ones as a function of  $n$ . For  $0.0 \leq n_{input} \leq 1.0$ , the mean value of  $dn$  is  $-0.01$  with an RMS of 0.04, and for  $3.0 \leq n_{input} \leq 4.0$ , the mean value of  $dn$  is  $-0.37$  with an RMS of 0.23. These results clearly establish that we are able to measure changes in the structure of Sérsic galaxies, and that galaxies with input  $n > 1$  cannot be mistaken for Sérsic galaxies.

#### 4. Comparison between Photometric Decomposition and Visual Classification

The HDF provides a unique database of galaxy images to study the morphological properties of a large sample of field galaxies. VDB96 has published a catalog of visually determined morphological classification for 19% of the galaxies in the field which can be compared to our quantitative classification. Such a comparison is important as it provides a direct link between the population of nearby galaxies and high redshift galaxies, and this link is essential to our understanding of the evolution of field galaxies. The classification done by VDB96 was based on the DDO system, a system defined through the young-star richness of the disk, the presence of a bar, the central concentration of light and the quality and length of the arms of the galaxy. A numerical system (Abraham *et al.* 1996b) accompanied the visual classification and was presented in VDB96. Objects such as peculiar galaxies or probable mergers were designated in the numerical system by the index  $vdB=7$  or 8. The rest of the numerical classification goes as follows: E/star:-1, E:0, E/S0/Sa:1, S0/Sa:2, Sa/Sab:3, Sb/S/Ir:4, Sc:5, and Ir:6.

VDB96 visually classified 271 galaxies in the HDF and derived the fractions of the different morphological types to be 30% ellipticals or lenticulars, 31% spirals or irregulars, and 39% unclassified galaxies. This fraction of HDF galaxies visually classified by VDB96 is displayed in Figure 12 along with our  $B/T$  parameter determination for comparison. Each galaxy is represented by a circle, and this circle scales with the measured half-light radius of the galaxy. If visual classification and our classification were in complete agreement, the points classified by VDB96 as elliptical galaxies would appear only in the upper left part of the diagram whereas the spirals should occupy only the lower right section. A significant fraction, i.e. 14%, of visually classified elliptical galaxies are systems with a  $B/T < 0.5$ . It is interesting to note that all the galaxies classified by VDB96 as lenticular galaxies have  $B/T < 0.5$ . The radially averaged profiles of some of the galaxies for which the VDB96 classification and ours differ are shown in Figure 13. As the profiles suggest, these galaxies are disk-dominated galaxies but classified by VDB96 as ellipticals. This difference in classification occurs for 40% of small round galaxies with half-light radii  $< 0''.31$ . The simulations indicate that GIM2D classifies these galaxies accurately (see Section 3.4). These small objects account partly for the fact that we obtain a smaller number of early morphological types than the one determined using visual morphological classification methods.

The VDB96 sample of galaxies has been classified by ABR96 using a quantitative classification system based on measurements of the central concentration and asymmetry of the galaxian light. The  $C - A$

classification developed by ABR96 is based on the results of Doi, Fukugita, & Okamura (1993) describing how central concentration and mean surface brightness can be used to distinguish between early and late Hubble types. The parameter  $C$  is the ratio of the flux between the inner and outer isophotes of normalized empirically defined radii measured from the intensity-weighted second-order galaxy image moments, and the parameter  $A$  is an asymmetry index measured by rotating and self-subtracting the galaxy image from itself. A plot of the  $C$  and  $A$  indices calculated by ABR96 is displayed in Figure 14. Each point is represented by a circle size proportional to the  $B/T$  value from GIM2D. For complete agreement, all the circles with  $B/T > 0.5$  should lie in the region of the diagram defined as E/S0 and the circles with  $B/T < 0.5$  should belong to the central region of the figure labeled SPIRAL. Although all the bulge-dominated galaxies except for four fall in the part of the diagram expected, some members of the disk-dominated population are classified as elliptical galaxies. Some, but not all, of these  $B/T < 0.5$  objects are the same objects identified by VDB96 as ellipticals.

There are four cases where bulge-dominated galaxies were classified as irregular/peculiar/merger (Irr/Pec/Mrg) in the  $C - A$  classification. These galaxies are in the upper left corner of Figure 14. The galaxies hd2\_0982\_1454 and hd4\_1589\_1175 have a companion which was identified in our sample as a separate object but where both objects were defined as one in the  $C - A$  classification, making them compact Irr/Pec/Mrg objects. They were both classified by VDB96 with a classification index  $\text{vdB}=8$ . The galaxy hd4\_1075\_1749 is part of a quadruplet. The grouping explains again the  $C - A$  classification. The VDB96 classification is  $\text{vdB}=0$ , consistent with a bulge-dominated galaxy. The galaxy hd4\_0281\_1323 has irregular features and therefore is classified by ABR96 as Irr/Pec/Mrg but classified by VDB96 as  $\text{vdB}=0$ , consistent with our classification of a bulge-dominated galaxy. It seems from this comparison that the VDB96 and ABR96 classifications do not consistently agree although they do agree in the instance that they are both classifying more galaxies as ellipticals than we find from our bulge/disk decomposition analysis.

## 5. Profile Anomalies in HDF Galaxies

The surface brightness profiles of most galaxies we have analyzed with GIM2D could be modeled with the classical combination of a de Vaucouleurs profile and an exponential profile. However, this model was insufficient to properly describe the photometric structure of a subsample of 82 Sérsic galaxies that were selected based on the criteria described in Section 3.4. The models of these galaxies converged to a pure exponential profile ( $B/T = 0$ ) with very small 99% confidence intervals. This behavior of the model indicated that the profiles of those “anomalous” galaxies were flatter than any possible realization of the classical model. These galaxies had profiles flatter than a pure exponential profile (see Figure 15) and could be described by a single-component Sérsic model with index  $0.2 \leq n \leq 1$ .

The observed profile anomalies can be real intrinsic structural anomalies or they can be caused by, say, a vigorously star-forming population with a distribution very different from the underlying galaxy profile. Although small perturbations on a smooth profile do not on average change the underlying profile parameters (see Section 3.3), large perturbations caused by merging, for example, can alter significantly the overall 2D profile shape. A blueing of the light from a pure disk galaxy in its central region can give rise to the kind of profile flattening observed in our subsample (see Figure 15) and yet have nothing to do with changes in the intrinsic structure of the galaxies. It was therefore important to determine which anomalous galaxies had color gradients and which ones did not. We created  $V - I$  color images of the anomalous galaxies by dividing the F606W HDF images by the corresponding F814W images. We derived  $V - I$

profiles by azimuthally averaging their surface brightness along isophotal ellipses with axial ratios calculated by SExtractor. Out of the 82 galaxies, 34 galaxies showed little or no color gradient ( $\delta(V - I) < 0.2$ ). The flat profiles of these galaxies thus represents real intrinsic structural anomalies. Figure 16 shows the distribution of Sérsic index values  $n$  for anomalous galaxies with no color gradient. The distribution has a median  $n$  value of 0.62 and a dispersion of 0.18. The Sérsic galaxies exhibit an interesting diversity of visual morphologies. Many are either mergers in progress or merger remnants as evidenced by tidal features such as tails. The amount of merging appears to vary significantly. Some mergers are between galaxies of roughly equal luminosities. Others look like “lit up Christmas trees”: many small, bright knots appear to be falling the potential well of a larger, central component. Figure 17 shows a mosaic of four representative Sérsic galaxy  $F814W$  images.

## 6. Discussion

We have fitted the surface brightness profiles of 1639 objects in the HDF and have obtained reliable quantitative morphological classification of 522 objects down to  $m_{F814W}(AB) = 26.0$ . The GIM2D classification has been tested through simulations and compared to the visual classification method of VDB96 and ABR96. Five effects were modeled: the galaxy selection function of the SExtractor detection algorithm, the parameter recovery success of GIM2D, the effect of asymmetric structures on the measured parameters, the selection criterion for galaxies with Sérsic profiles, and the recovery success of the Sérsic index for these galaxies. We found that incompleteness was not a major problem down to the above magnitude limit. However, the galaxy selection function showed a clear bias against pure disk systems whereas all bulge-dominated galaxies appeared to have been found. This bias is due to the disk profile being less concentrated than the bulge profile. The following results have emerged from the simulations and profile analysis of HDF galaxies.

The dominant contribution to the galaxy population in the HDF comes from the disk-dominated galaxies. There are no large ( $r_{hl} \geq 0''.7$ ) bulge-dominated systems in our sample of the HDF, and the fraction of bulge-dominated galaxies ( $B/T > 0.5$ ) down to  $m_{F814W}(AB) = 26.0$  is 8%. This is a much smaller percentage than found by VDB96 and ABR96 with visual classification. The discrepancy is even more pronounced if we associate VDB96’s E/S0 systems with  $B/T > 0.8$ . We find that the discrepancy between our low percentage of early-type galaxies and the larger percentage found by visual classification is due to the difference in classification of 40% of small round galaxies with half-light radii  $< 0''.31$ . Although these objects are visually classified as elliptical galaxies, we find that they are disk-dominated with bulge fractions  $< 0.5$ . The simulations indicate that GIM2D classifies these galaxies accurately.

This result emphasizes two obvious problems of visual classification. First, the visual method is neither reliable nor reproduceable. In general, the subjectivity of visual classification makes it impossible to measure or even simply determine in a consistent way the systematic errors associated with this type of classification. Second, our quantitative system of classification is based on a set of measurements that only roughly maps onto the DDO system due to the fact that  $B/T$  is an important component of that system. Our different classification results on the HDF suggest that profile shape has only a very indirect relationship with visual morphological classification. It is not possible to map galaxies directly onto the DDO system by measuring profile parameters. Therefore, it is difficult to compare samples of distant and nearby galaxies, which have predominantly been classified visually.

Assuming a one-to-one correspondence between visual and bulge/disk classification for the nearby

sample of galaxies, we compare our revised number for the frequency of morphological types in the HDF with the local sample as quoted in VDB96. Since the HDF galaxy redshift distribution peaks at  $z \sim 0.5$  (Cohen *et al.* 1996), we are measuring a *decrease* in the number of bulge-dominated galaxies as a function of look-back time. This agrees with the absence of passively evolving ellipticals in deep optical and near-infrared surveys (Zepf 1997). Up to a redshift of  $z \sim 1$ , stellar synthesis models (Bruzual & Charlot 1993) predict that the elliptical galaxies should stay red in  $V - I$  color and therefore should not be disappearing from our sample at these low redshifts, unless they form in environments containing a significant amount of dust. If real, this decrease may be due to merging and at least some of the elliptical galaxies will be formed by the coalescence of colliding galaxies of different morphological types. It is also possible that spheroids form by the collapse of many subclumps (Kauffmann *et al.* 1993; Navarro *et al.* 1995; Cole *et al.* 1994) and that these subclumps and substructure have different morphologies. By collecting color as well as morphological information for the HDF galaxies, it is possible to determine if the morphological evolution is also responsible for the excess number of blue galaxies at faint magnitudes in redshift surveys or if a single population of galaxies is evolving in color. This study, including the use of redshift information available now on the HDF galaxies, will make up the content of a future paper.

With redshift information, we can study the morphological evolution of galaxies and test the claim that high redshift galaxies are in general very compact, with  $r^{1/4}$  law radial profiles, and with scales comparable to the cores of present-day luminous galaxies (Giavalisco *et al.* 1996a; Giavalisco *et al.* 1996b; Steidel *et al.* 1996a; Steidel *et al.* 1996b). Because of these properties, these galaxies are thought to be most likely the progenitors of bulges or normal elliptical galaxies. The  $z > 3$  galaxies with measured spectroscopic redshifts of Lowenthal *et al.* (1997) have small sizes, with half-light radii in the range 1.5-3  $h_{50}^{-1}$  kpc (for  $q_0 = 0.05$ ), but show a wide range of morphologies. As Lowenthal *et al.* (1997) suggest, the small sizes of these objects and their morphology are also consistent with other scenarios of galaxy formation and evolution. The substructure seen in some objects could be due to the hierarchical formation of the galaxy beginning with subclumps or they could be isolated knots of star formation.

If all the high redshift ( $z > 2$ ) objects are indeed bulge-dominated galaxies, it appears from our analysis that the morphological distribution of galaxies in the HDF does not agree with these findings. In Figure 18, we present the bulge fraction of the sample of 61 galaxies with measured spectroscopic redshifts (Cohen *et al.* 1996, Lowenthal *et al.* 1997, Steidel *et al.* 1996a, and Zepf *et al.* 1997). The lack of objects between  $z \sim 1 - 2$  is due to the observing strategy and target selection of the different groups and the difficulty of spectral identification. All the galaxies range in sizes from  $r_{hl} = 0''.10$  to  $r_{hl} = 1''.12$  and have redshifts from  $z = 0.129$  to  $z = 3.368$ . Assuming  $q_0 = 0.5$ , the 15 objects with  $z > 2.0$  have half-light radii in the range 0.73-2.99  $h_{50}^{-1}$  kpc and only one third of the objects are bulge-dominated galaxies. Of these bulge-dominated galaxies, hd4\_1588\_1174, the largest, is at redshift  $z = 2.803$  with size  $r_e = 4.19 h_{50}^{-1}$  kpc, comparable to the size of a normal elliptical galaxy (Bender *et al.* 1992). The smallest bulge at  $z = 3.21$ , hd4\_1075\_1749, which is part of a quadruplet (see Section 4), has  $r_e = 1.63 h_{50}^{-1}$  kpc, corresponding to the size of a dwarf elliptical. These two galaxies have high luminosities  $L > L^*$  (Lowenthal *et al.* 1997). The objects selected by Lowenthal *et al.* (1997) are at  $z > 2.0$  and have  $B/T \leq 0.54$ . All but two have  $B/T < 0.2$ , so the majority of these galaxies have dominant exponential profiles and do not fit the description of cores of proto-spheroids unless they merge later on to form elliptical galaxies. These objects are small compared with present day disks, with a range in their half-light radii of 0.73-2.60  $h_{50}^{-1}$  kpc.

We have found 82 galaxies with profiles shallower than an exponential profile. Fitting pure Sérsic profiles to those objects and excluding those with large color gradient, we found that the Sérsic indices of the remaining 34 galaxies had a median value of 0.62 and a dispersion of 0.18. Many of these Sérsic galaxies

shows evidence of mergers. We intend to study these Sérsic galaxies in greater details in a future paper.

The outcome of our analysis on the HDF images are summarized here: (1) Our morphological analysis of 522 galaxies in the field indicates that the spheroidal or bulge-dominated galaxies make up for only a small fraction, i.e. 8%, of the galaxy population down to  $m_{F814W}(AB) = 26.0$ . (2) We showed that the large fraction of early-type systems in the VDB96 and ABR96 sample is due to the difference in classification of small round galaxies with half-light radii  $< 0''.31$ . Although these objects are visually classified as elliptical galaxies, we find that they are disk-dominated with bulge fractions  $< 0.5$ . (3) We found a majority of disk-dominated galaxies in our high redshift ( $z > 2$ ) sample and only a small fraction of spheroids. (4) We observed galaxies with profiles flatter than a pure exponential profile and many of these objects show signs of merging.

F.R.M. would like to acknowledge support from the HST NASA grant #AR-07523.01 provided by T.J. Broadhurst. L.S. gratefully acknowledges financial support from the Natural Sciences and Engineering Research Council of Canada through a Postdoctoral Fellowship and support from HST grant #AR 06337.08-94A by D.C Koo. We would like to thank M. Bolte, J.R. Graham and A.C. Phillips for helpful discussions and comments. We are also grateful to our referee R.G. Abraham for his comments and suggestions on improving the paper.

## REFERENCES

- Abraham, R.G., Tanvir, N.R., Santiago, B.X., Ellis, R.S., Galzebrook, K., & van den Bergh, S. 1996a, MNRAS, 279, L47 (ABR96)
- Abraham, R.G., van den Bergh, S., Glazebrook, K., Ellis, R., Santiago, B.X., Surma, P., & Griffiths, R.E. 1996b, ApJS, 107, 1
- Abraham, R.G., Valdes, F., Yee, H.K.C., & van den Bergh, S. 1994, ApJ, 432, 75
- Bertin, E., & Arnouts, S. 1996, A&AS, 117, 393
- Bouwens, R.J., Broadhurst, T.J.B., & Silk, J. 1997, astro-ph/9710291
- Bruzual, A., & Charlot, S. 1993, ApJ, 405, 538
- Capaccioli, M. 1989, in Corwin H.G., Bottinelli L., eds, The World of Galaxies, Springer-Verlag, Berlin, p.208
- Cohen, J.G., Cowie, L.L., Hogg, D.W., Songaila, A., Blandford, R., Hu, E.M. & Shopbell, P. 1996, ApJ, 471, L5
- Cowie, L.L., Songaila, A., Hu, E.M., & Cohen, J.G. 1996, AJ, 112, 839
- de Vaucouleurs, G. 1948, Ann. d'Ap., 11, 247
- de Vaucouleurs, G. 1953, MNRAS, 113, 134
- de Vaucouleurs, G. 1956, Occasional Notes RAS, 3, 129
- de Vaucouleurs, G. 1959, in Handbuch der Physik, 53, ed. S. Flugge (Berlin: Springer), 275
- Ellis, R.S., Colless, M., Broadhurst, T., Heyl, J., & Glazebrook, K.G. 1996, MNRAS, 280, 235
- Giavalisco, M., Livio, M., Bohlin, R.C., Macchetto, F.D., & Stecher, T.P. 1996a, AJ, 112, 369
- Giavalisco, M., Steidel, C.C., & Macchetto, F.D. 1996b, ApJ, 470, 189

- Hubble, E. 1926, ApJ, 64, 321
- Hubble, E. 1930, ApJ, 71, 231
- Kauffmann, G., Charlot, S., & White, S.D.M. 1996, MNRAS, 283, L117
- Krist, J. 1993, in *Astronomical Data Analysis Software and Systems II*, 52, eds. R. J. Hanisch, R. J. V. Brissenden, & Jeannette Barnes (A.S.P. Conference Series), 536
- Lilly, S.J., Tresse, L., Hammer, F., Crampton, D., & Le Fèvre, O. 1995, ApJ, 455, 108
- Lowenthal, J.D., Koo, D.C., Guzmán, R., Gallego, J., Philips, A.C., Faber, S.M., Vogt, N.P., Illingworth, G.D., & Gronwall, C. 1997, ApJ, 481, 673L
- Metropolis, N., Rosenbluth, A., Rosenbluth, M., Teller, A., and Teller, E. 1953, *Journal of Chemical Physics*, 21, 1087
- Okamura, S., Watanabe, M., & Kodaira, K. 1988, in *The World of Galaxies*, ed. H. Corwin & L. Bottinelli (Berlin: Springer), 75
- Patterson, F.S. 1940, *Harvard Bull.*, 914, 9
- Sandage, A. 1961, *Hubble Atlas of Galaxies* (Washington: Carnegie Inst. Washington)
- Saha, P., & Williams, T.B. 1994, AJ, 107, 1295
- Schade, D., Lilly, S.J., Crampton, D., Hammer F., Le Fèvre, O., & Tresse L. 1995, ApJ, 451, 1
- Schade, D., Lilly, S.J., Le Fèvre, O., Hammer, F., & Crampton, D. 1996, ApJ, 464, 79
- Sérsic, J.L. 1968, *Atlas de Galaxias Australes* (Cordoba: Observatorio Astronomica)
- Simard, L. 1998, in preparation
- Steidel, C.C., Giavalisco, M., Dickinson, M.E., & Adelberger, K.L. 1996a, AJ, 112, 352
- Steidel, C.C., Giavalisco, M., Pettini, M., Dickinson, M.E., & Adelberger, K.L. 1996b, ApJ, 462, L17
- Steinmetz, M., & Müller, E. 1995, MNRAS, 276, 549
- van den Bergh, S., Abraham, R.G., Ellis, R.S., Tanvir, N.R., & Glazebrook, K.G. 1996, AJ, 112, 359 (VDB96)
- Vanderbilt, D., & Louie, S.G. 1984, *Journal of Computational Physics*, 56, 259
- Williams, R.E. *et al.* 1996, AJ, 112, 1335
- Zepf, S.E., Moustakas, L.A., & Davis, M. 1997, ApJ, 474, L1
- Zepf, S.E. 1997, astro-ph/9711355

Fig. 1.— *Left*: The top left quarter of the WFPC2-chip 4 F814W HDF image, displaying a field of view of  $36''.8 \times 36''.0$ . *Right*: The residual image created by GIM2D after detailed bulge/disk decompositions have been performed on all galaxies in the field.

Fig. 2.— Observed structural parameter distributions of the HDF galaxies for all 1639 objects analyzed with GIM2D. All distributions except  $N(m_{F814W}(AB))$  have been normalized by the total number of objects in our catalog (1639 objects).  $N(m_{F814W}(AB))$  is in  $\text{mag}^{-1} \text{deg}^{-2}$ .

Fig. 3.— Observed structural parameter distributions of the HDF galaxies with  $m_{F814W}(AB) \leq 26.0$ . All distributions except  $N(m_{F814W}(AB))$  have been normalized by the total number of objects in our catalog (1639 objects).  $N(m_{F814W}(AB))$  is in  $\text{mag}^{-1} \text{deg}^{-2}$ .

Fig. 4.— Half-light radius distributions of the HDF galaxies for different  $m_{F814W}(AB)$  cuts. All distributions have been normalized by the total number of objects in our catalog (1639 objects). Clockwise from top left-hand corner:  $N(r_{hl})$  for all 1639 objects,  $N(r_{hl})$  for  $m_{F814W}(AB) \leq 26.0$ ,  $r_{hl}$  versus  $B/T$  for  $21.0 \leq m_{F814W}(AB) \leq 22.6$  (filled circles),  $22.6 < m_{F814W}(AB) \leq 24.0$  (pluses),  $24.0 < m_{F814W}(AB) \leq 26.0$  (crosses),  $N(r_{hl})$  for  $24.0 < m_{F814W}(AB) \leq 26.0$ ,  $N(r_{hl})$  for  $22.6 < m_{F814W}(AB) \leq 24.0$ ,  $N(r_{hl})$  for  $21.0 < m_{F814W}(AB) \leq 22.6$ .

Fig. 5.— Contour plot of the SEXtractor selection function  $S(\omega)$  as a function of the F814W half-light radius  $r_{hl}$  and the total F814W AB magnitude for the HDF.  $S(\omega)$  was constructed with 66000 galaxy models spanning a wide range of structural parameters. The detection threshold was  $1.5\sigma$ , and the minimum object detection area was 30 pixels.

Fig. 6.— Observed (*solid histogram*) and intrinsic (*dashed histogram*) structural parameter distributions for  $m_{F814W}(AB)$ ,  $B/T$ , and  $r_{hl}$  calculated over the range  $21.0 < m_{F814W}(AB) \leq 29.0$  for  $S_{lim} = 0.1$  (*top*) and  $S_{lim} = 0.5$  (*bottom*). Notice that objects with magnitudes down to  $m_{F814W}(AB) = 28.0$  are detected for the  $S_{lim} = 0.1$  but for the most stringent limit of  $S_{lim} = 0.5$ , only objects in the brighter bins with  $m_{F814W}(AB) \leq 26.0$  are detected.

Fig. 7.— Observed (*solid histogram*) and intrinsic (*dashed histogram*) structural parameter distributions for  $m_{F814W}(AB)$ ,  $B/T$ , and  $r_{hl}$  calculated over the range  $21.0 < m_{F814W}(AB) \leq 26.0$  for  $S_{lim} = 0.1$  (*top*) and  $S_{lim} = 0.5$  (*bottom*).

Fig. 8.— *Left*: Asymmetric residual fluxes index  $R_A$  as a function of  $B/T$  for our sample of 522 HDF galaxies with  $m_{F814W}(AB) \leq 26.0$ .  $R_A$  is computed using an aperture of size  $2r_{hl}$  and remains smaller than  $\sim 20\%$  for the majority of galaxies. *Right*: A measure of the residual fluxes  $\chi_R^2$  as a function of the degree of asymmetry  $R_A$  for the same sample of galaxies.

Fig. 9.— *Left*: Example of a  $2''.4 \times 2''.4$  simulated galaxy image with asymmetric features parametrized by  $F_b = 0.10$ ,  $n_b = 5$  and  $r_b = 1.5r_{hl}$ . The simulations were generated for the smooth component parameters  $m_{F814W}(AB) = 24.0$ ,  $B/T = 0.3$ ,  $r_e = 0''.12$ ,  $e = 0.2$ ,  $r_d = 0''.32$ ,  $i = 20^\circ$ ,  $\phi_b = \phi_d = 60^\circ$ , and  $n = 4.0$ . *Right*: Mean measured  $B/T$  with  $1\sigma$  error bars for the asymmetric parameters  $n_b = 5$ ,  $r_b = 1.5r_{hl}$  and the five discrete flux levels  $F_b = 0.0, 0.05, 0.10, 0.15, 0.20$ .

Fig. 10.— *Top and left*: The difference  $d(B/T)$  between measured and input bulge fractions versus seeing-deconvolved half-light radius for three different bulge fraction intervals ( $0.0 < B/T \leq 0.2$  (solid circles),  $0.2 < B/T \leq 0.8$  (open triangles), and  $0.8 < B/T$  (crosses)). *Top and right*: Mean difference  $d(B/T)$  between measured and input bulge fractions versus seeing-deconvolved half-light radius with  $1\sigma$  error bars. *Bottom*



and left: The difference  $d(B/T)$  between measured and input bulge fractions versus the input bulge fraction. *Bottom and right:* Mean difference  $d(B/T)$  between measured and input bulge fractions versus input bulge fraction with  $1\sigma$  error bars. All simulations with  $m_{F814W}(AB) \leq 26.0$  were included.

Fig. 11.— *Top:* Difference  $dn$  between measured and input Sérsic indexes versus input Sérsic index obtained by fitting pure Sérsic models to 300 pure Sérsic profile simulations. *Bottom:* Measured bulge fraction  $B/T$  versus input Sérsic index  $n$  obtained by fitting bulge/disk model to 300 pure Sérsic profile simulations. All simulations with  $m_{F814W}(AB) \leq 26.0$  were included.

Fig. 12.— Comparison of the parameter  $B/T$  with the morphological type  $\text{vdB}$  derived from VDB96. The size of the circles is proportional to  $r_{hl}$ . If visual classification and our classification were in complete agreement, the points classified by VDB96 as elliptical galaxies would appear only in the upper left part of the diagram whereas the spirals should occupy only the lower right section.

Fig. 13.— Examples of the difference in classification of small round galaxies. The three rows, from top to bottom, are the radially averaged surface brightness profiles of the galaxy `hd4_1413_0805`, `hd4_1815_0519` and `hd4_0894_1692`. The points are drawn with their  $1\sigma$  Poissonian error bars. They are assigned a VDB96 classification type  $\text{vdB}=0$  but a bulge/disk decomposition suggests increasing values of  $B/T = 0.0029, 0.2833$  and  $0.3365$ . These galaxies are clearly dominated by an exponential profile component and the difference in classification appears related to the fact that these galaxies are small and round, with  $r_{hl} = 0''.31, 0''.12$  and  $0''.25$ , respectively.

Fig. 14.— Comparison with the  $C - A$  classification of ABR96. The triangles and circles represent objects with  $B/T \leq 0.5$  and  $B/T > 0.5$ , respectively, with sizes proportional to  $B/T$ . The dotted triangles are for galaxies with  $B/T < 0.5$  but classified by VDB96 as  $\text{vdB}=0$ .

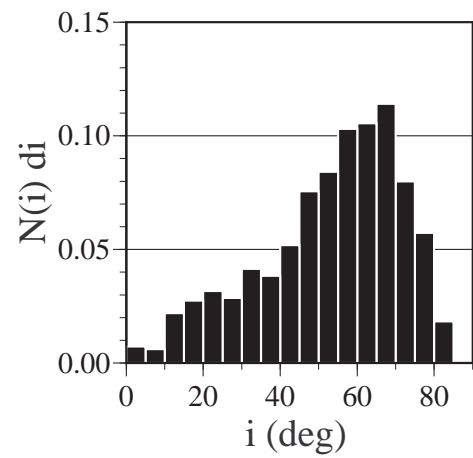
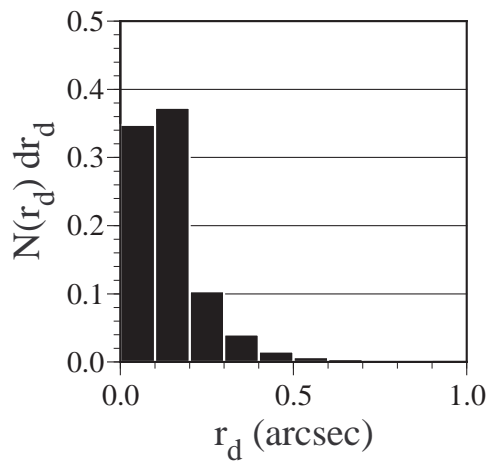
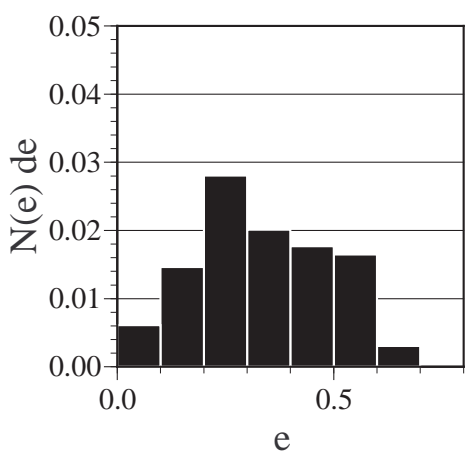
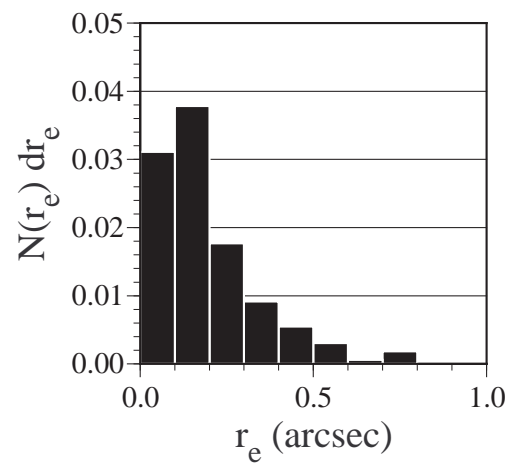
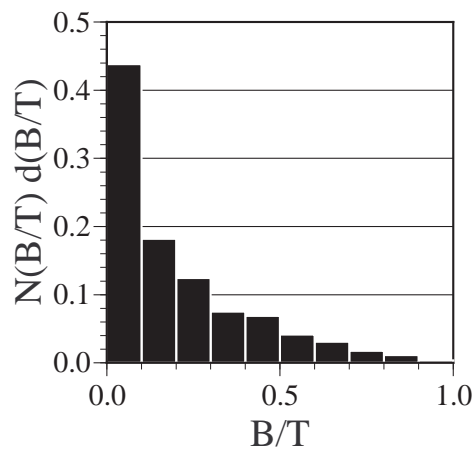
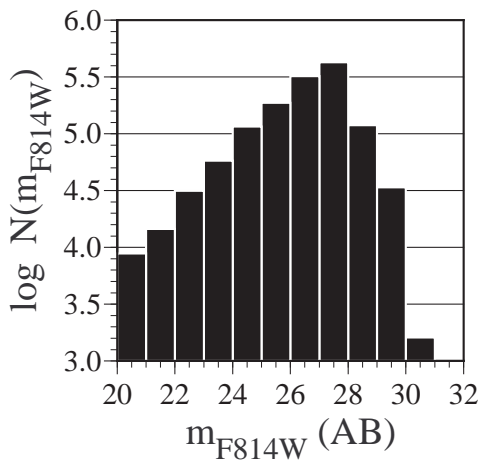
Fig. 15.— From top to bottom, examples of photometric profiles flatter than a pure exponential for the galaxies `hd3_0528_0623`, `hd4_0487_0790`, `hd4_0228_1931`, and `hd3_0353_1404`. The points are drawn with their  $1\sigma$  Poissonian error bars. The flatness of the profile in the F814W-band is due in two cases to a color gradient (top) but in the other two cases, the flattening occurs as a real structural property of the galaxy (bottom).

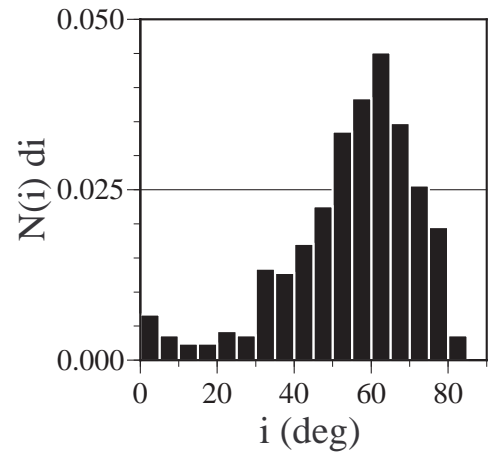
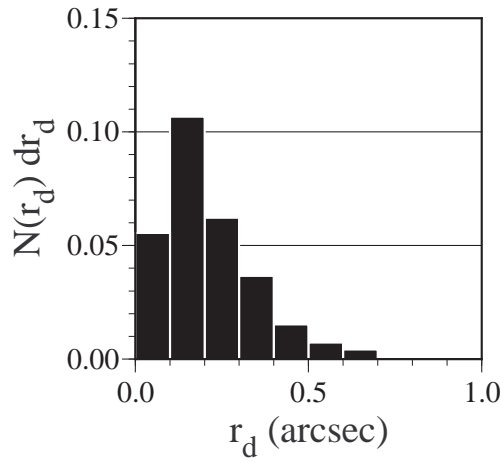
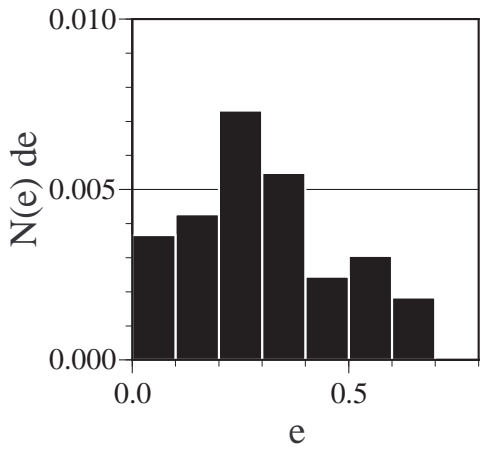
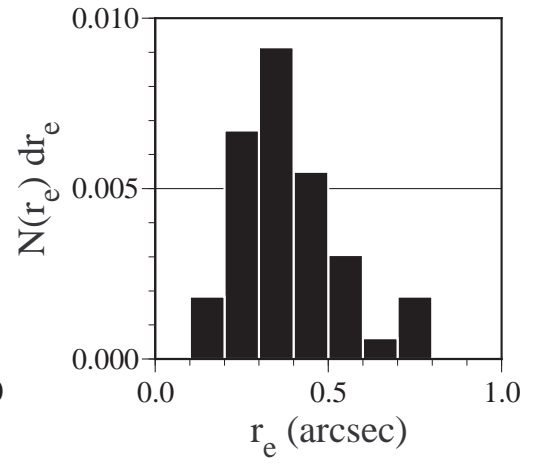
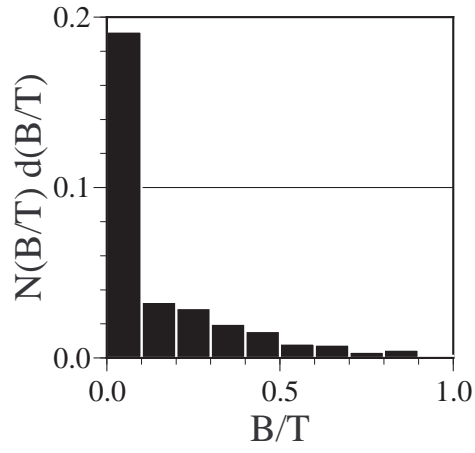
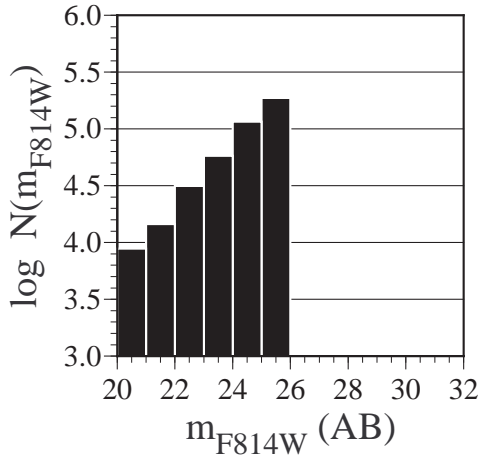
Fig. 16.— Distribution of Sérsic index values for Sérsic galaxies with no color gradient ( $\delta(V - I) < 0.2$ ). The median value of  $n$  is 0.62, and the dispersion  $\sigma_n = 0.18$ .

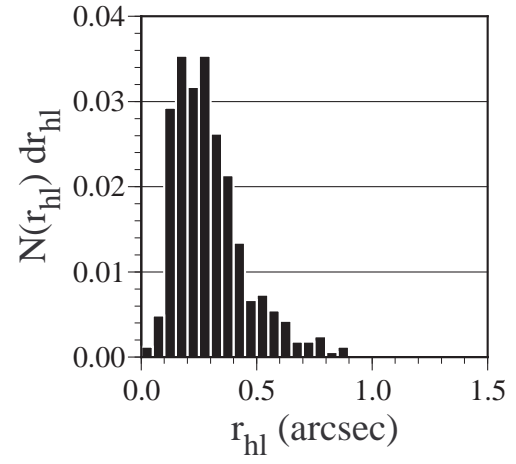
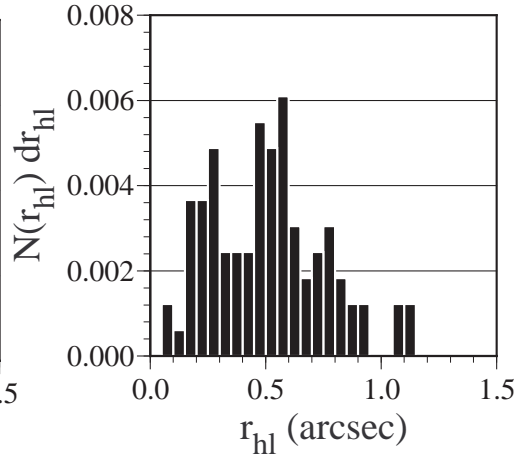
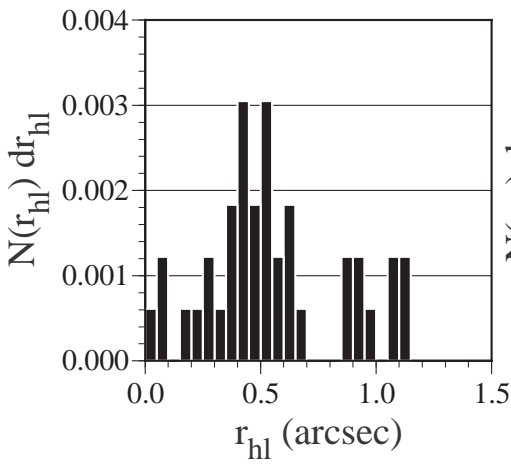
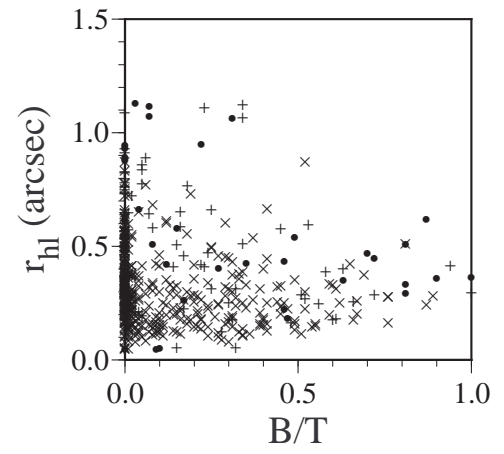
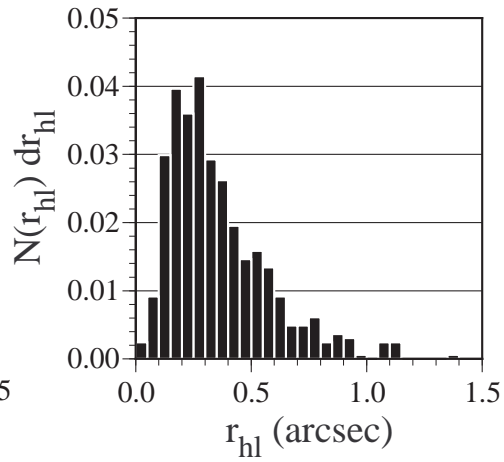
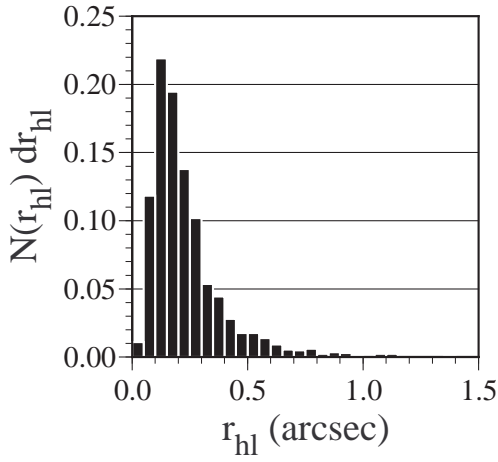
Fig. 17.— Mosaic image of four structurally anomalous galaxies in the F814W filter. As these images show, the anomalous galaxies appear either as compact looking mergers or more diffuse galaxies with surface brightness nebulosities. The galaxies `hd4_1187_0311` and `hd3_0353_1404`, the latter appearing in Figure 15, have no color gradient. The scale of these images is of  $7''.56$  on a side. The objects themselves have half-light radii  $r_{hl} < 0''.5$ .

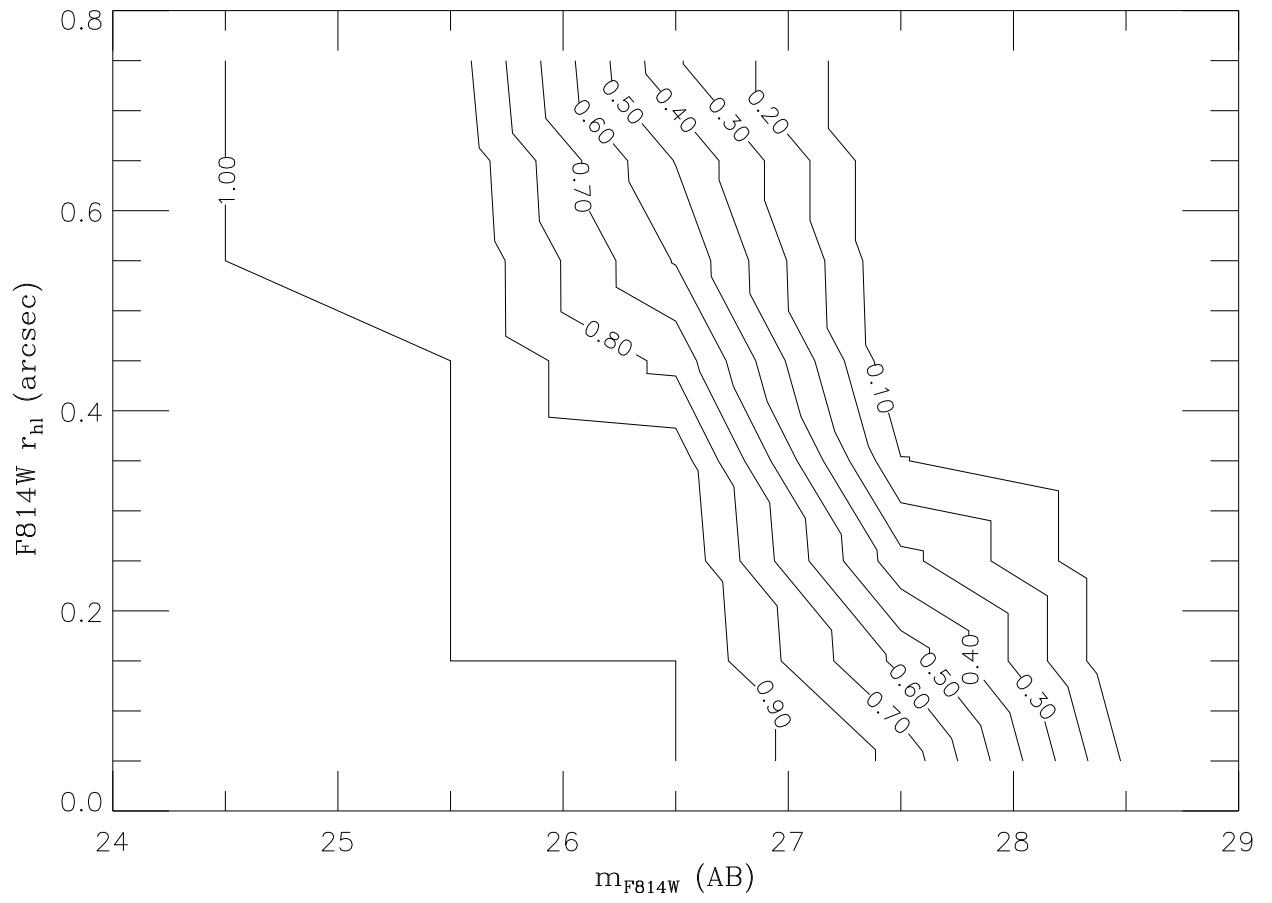
Fig. 18.— Bulge fraction as a function of redshift for 61 galaxies with published spectroscopic redshifts. The 99% confidence limits of the bulge fraction parameter are shown with error bars. The points denoted by crosses are the spectroscopic redshifts from Cohen *et al.* (1996), Steidel *et al.* (1996a), and Zepf *et al.* (1997) and the filled circles are from Lowenthal *et al.* (1997). The objects selected by Lowenthal *et al.* (1997) are at  $z > 2.0$  and have  $B/T < 0.45$  except for one galaxy with  $B/T = 0.54$ . All the galaxies range in size from  $0''.10 < r_{hl} < 1''.12$ . The objects with  $z > 2.0$  have half-light radii in the range  $2.06\text{-}9.28 h_{50}^{-1}$  kpc.

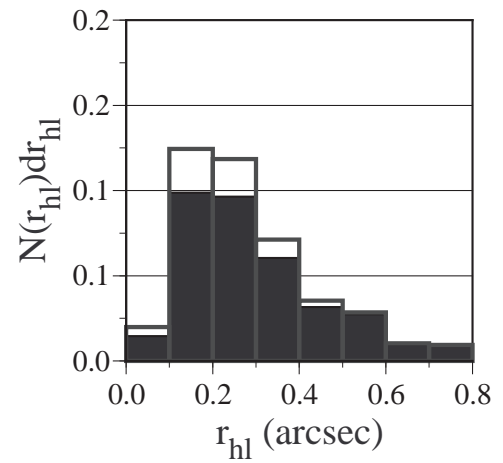
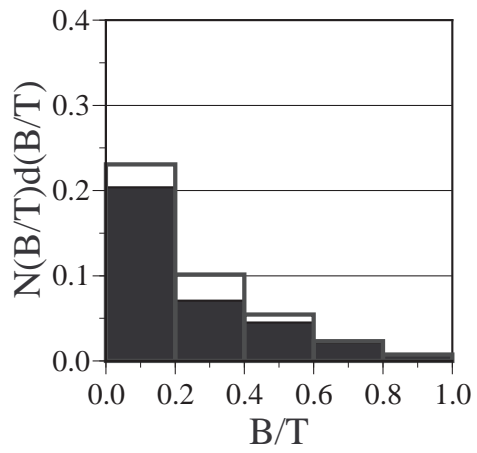
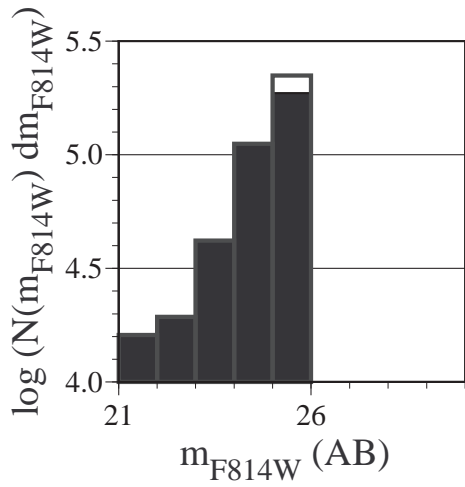
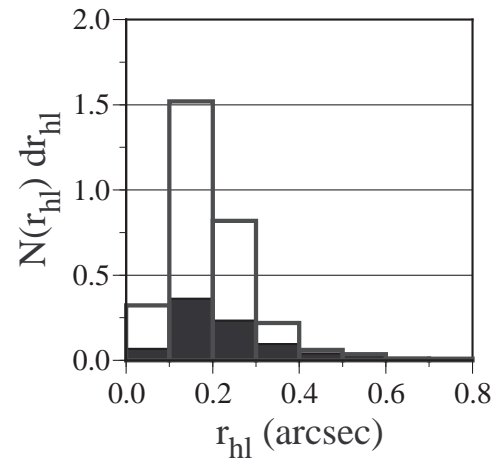
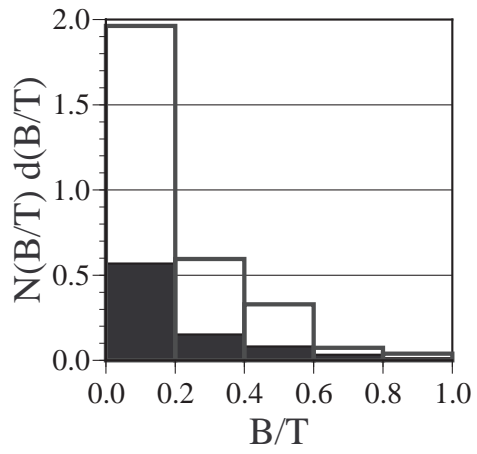
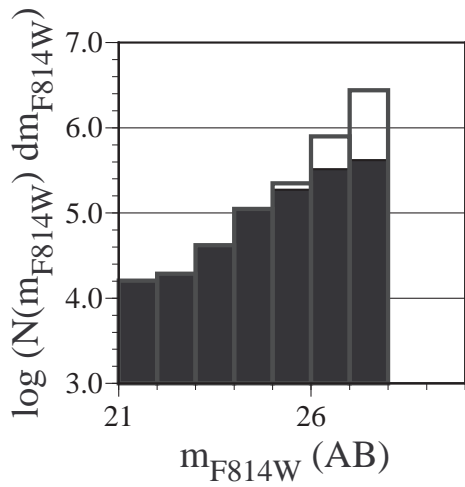


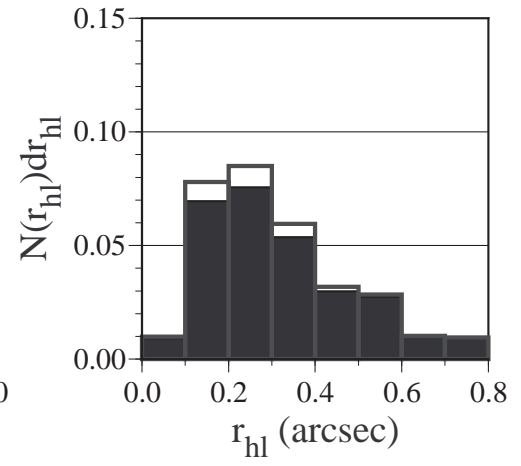
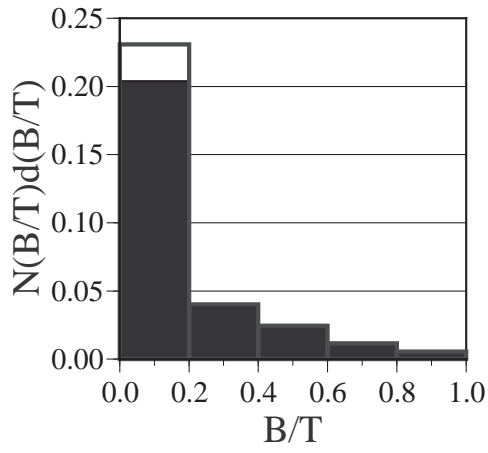
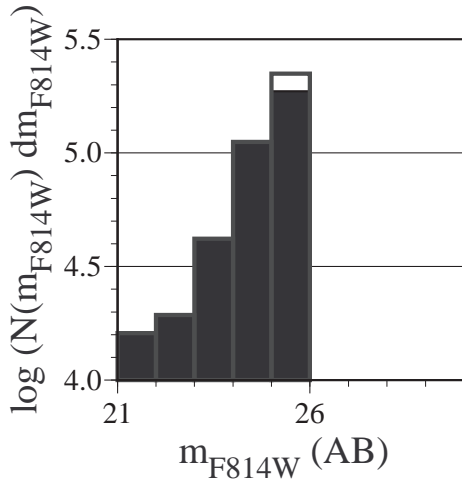
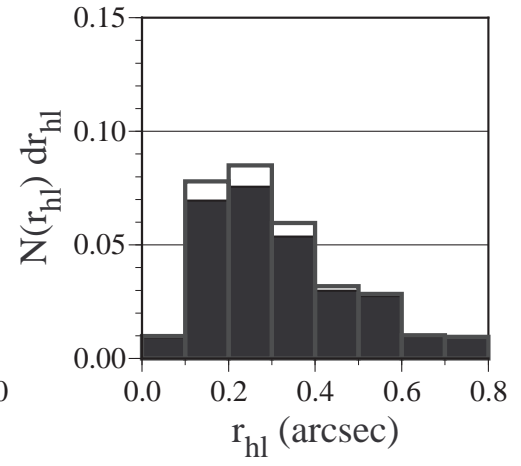
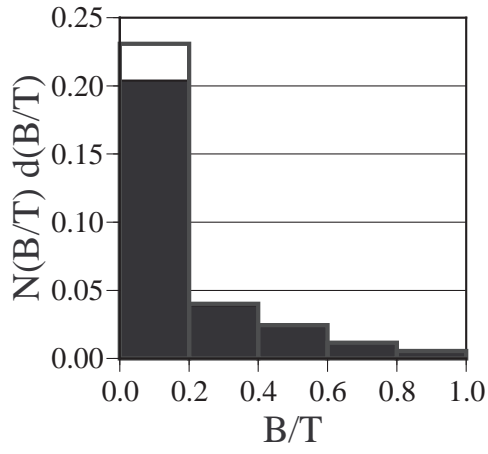
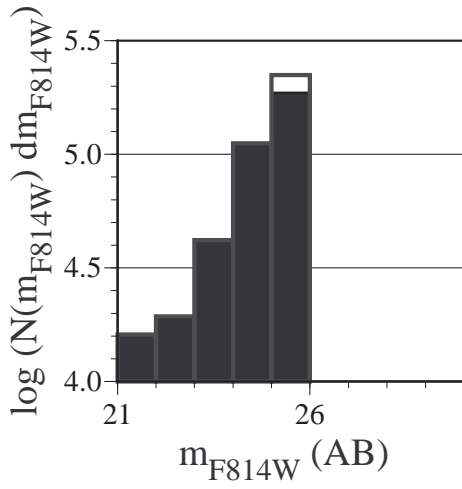




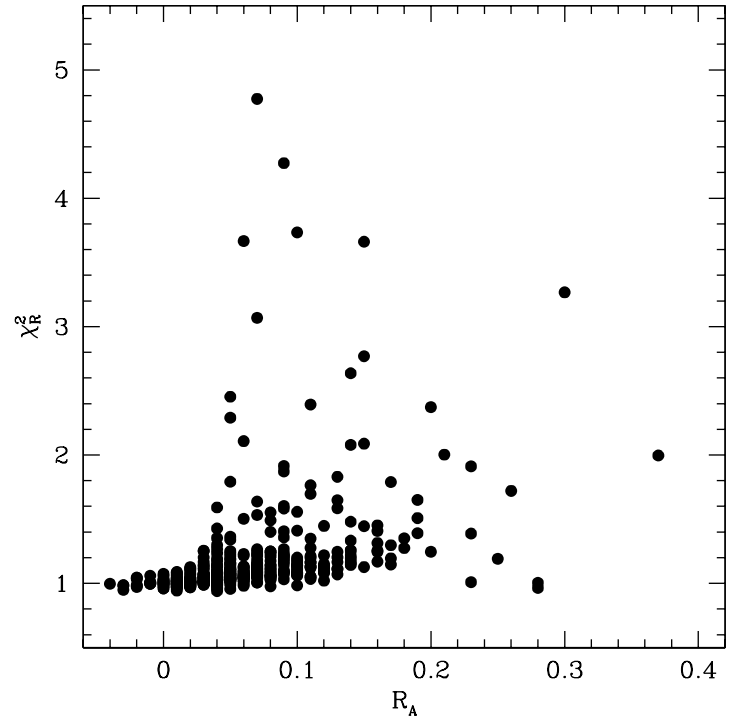
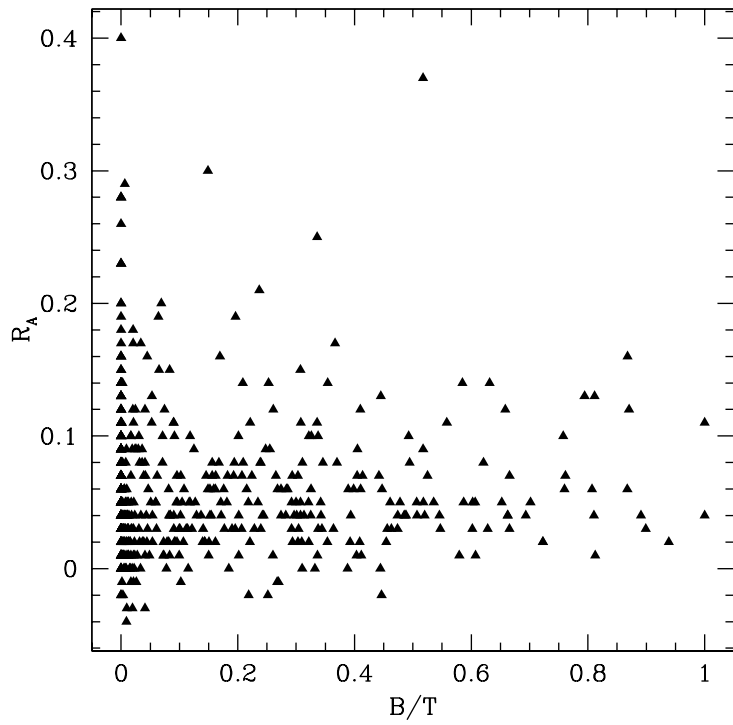


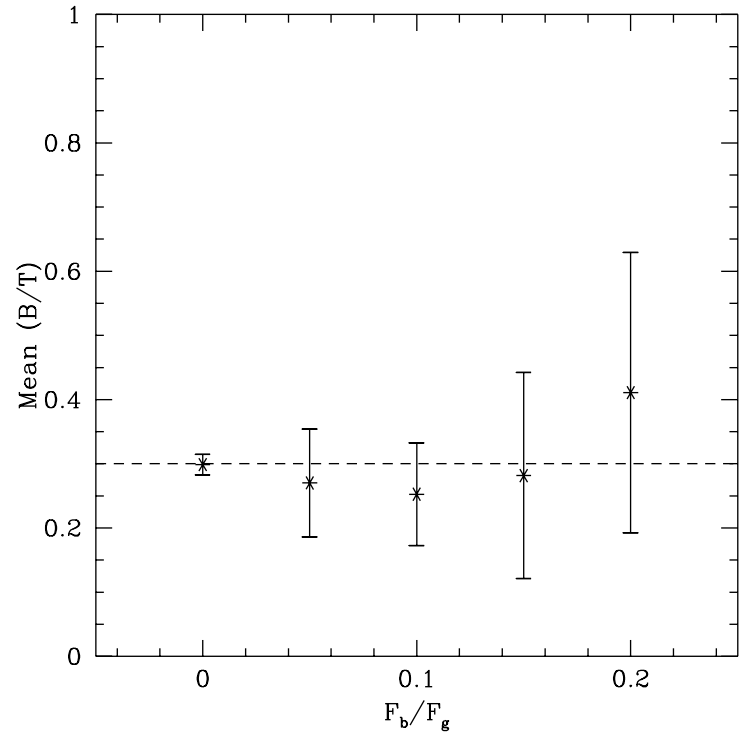
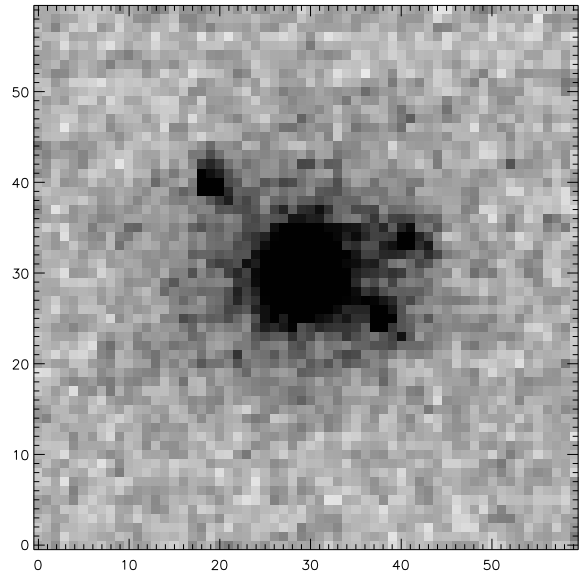


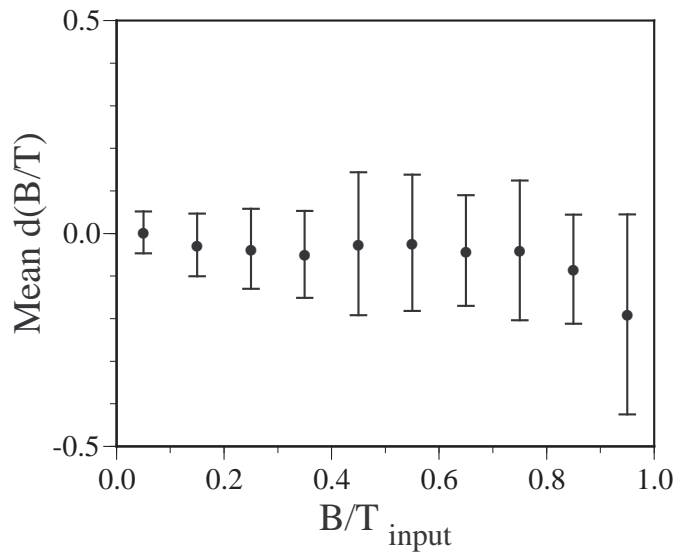
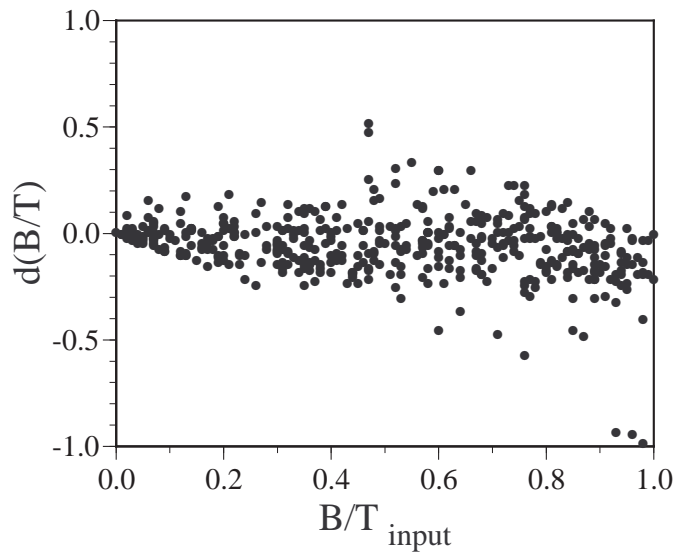
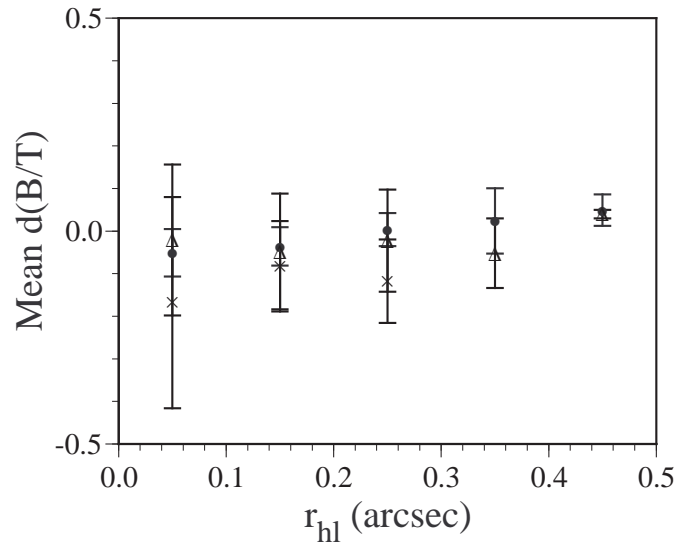
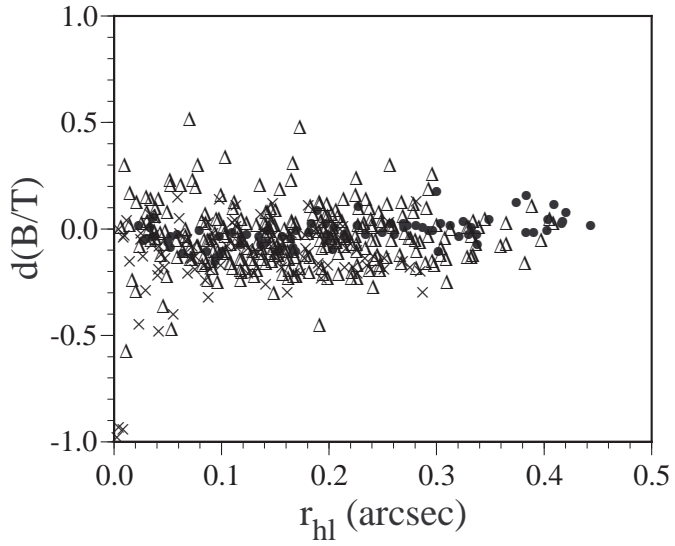


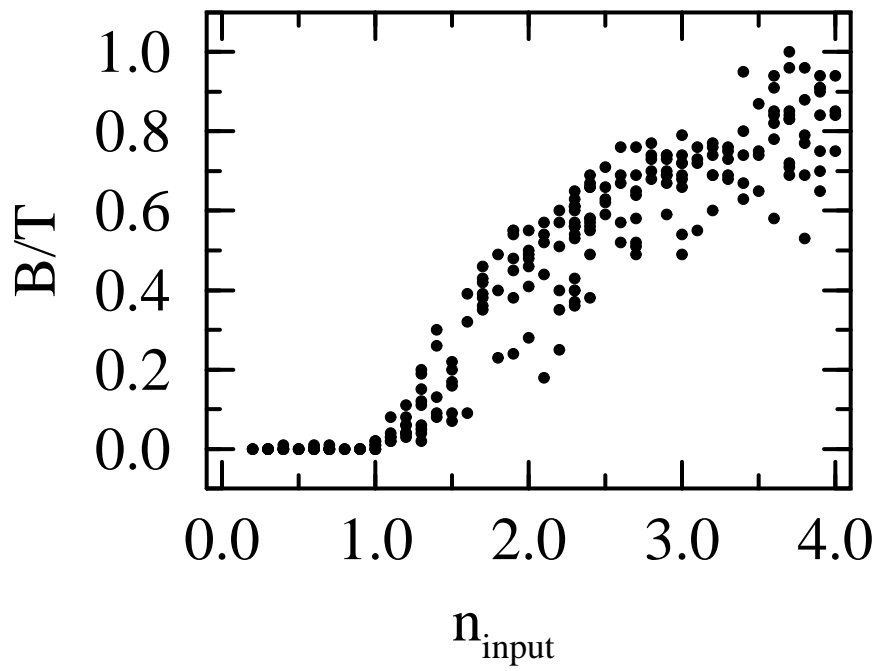
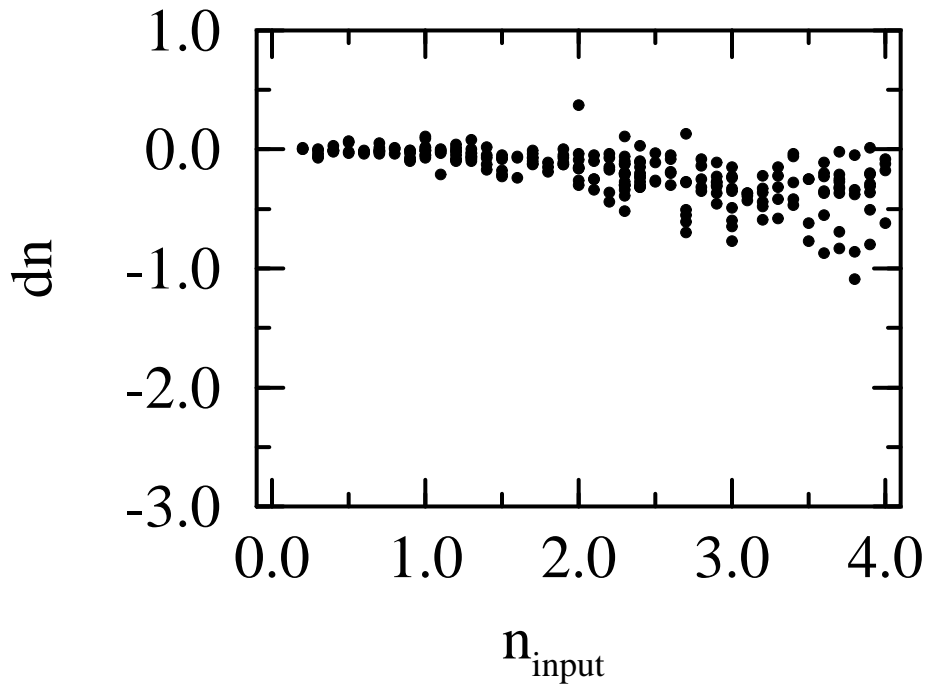


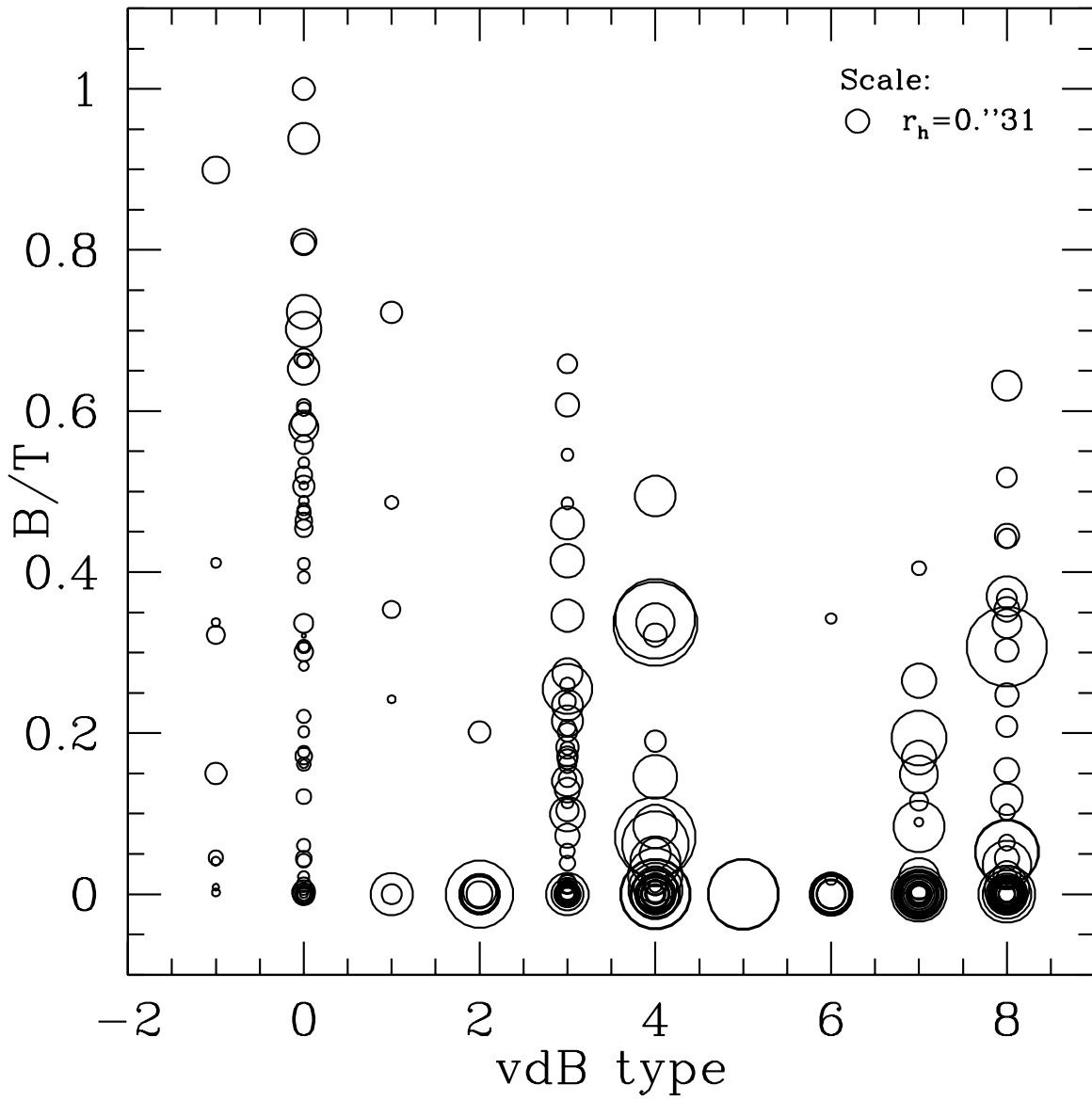




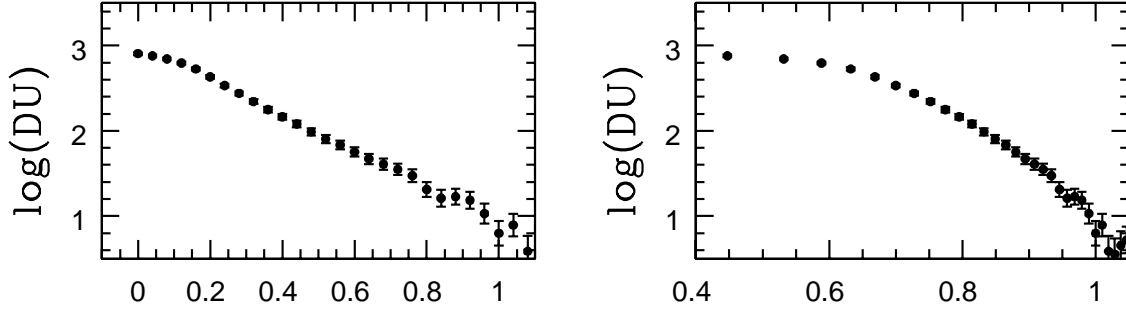




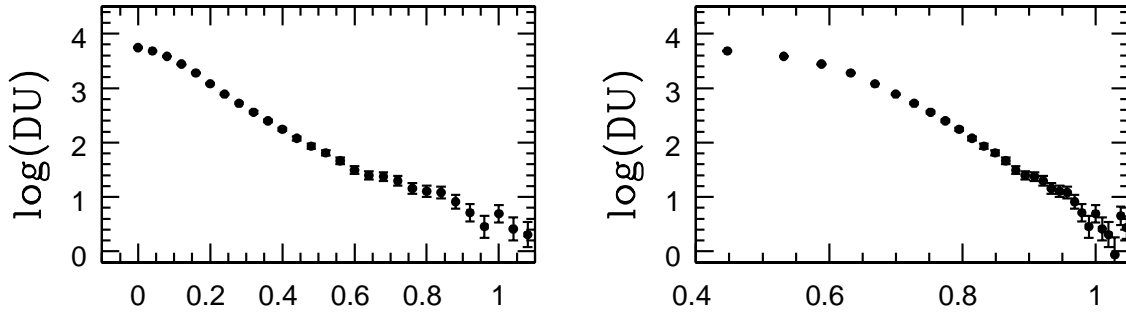




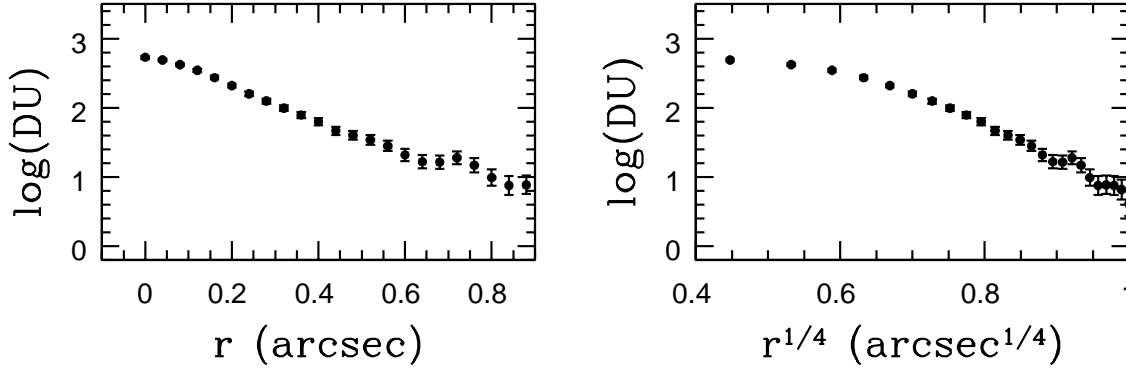
hd4\_1413\_0805

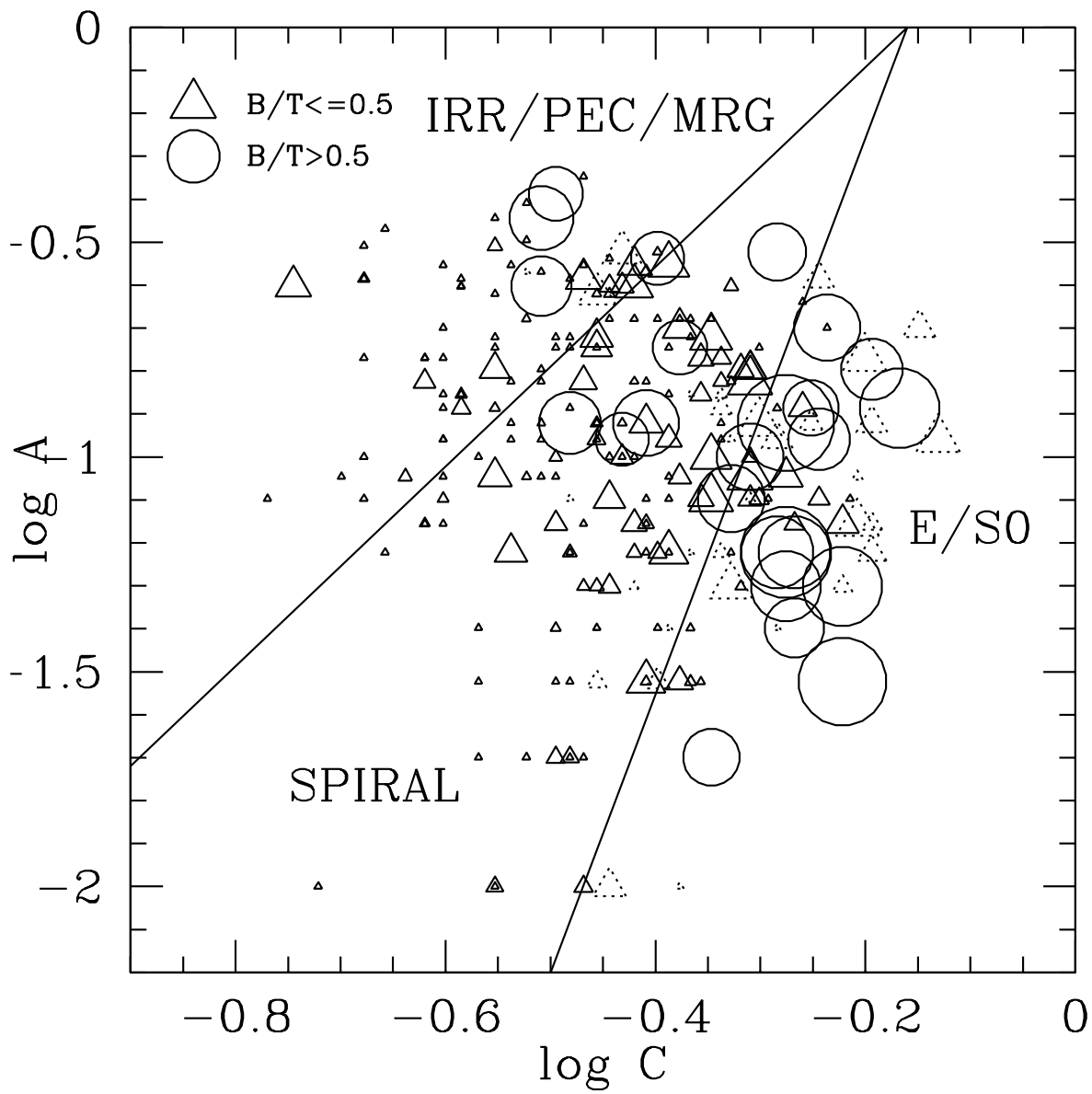


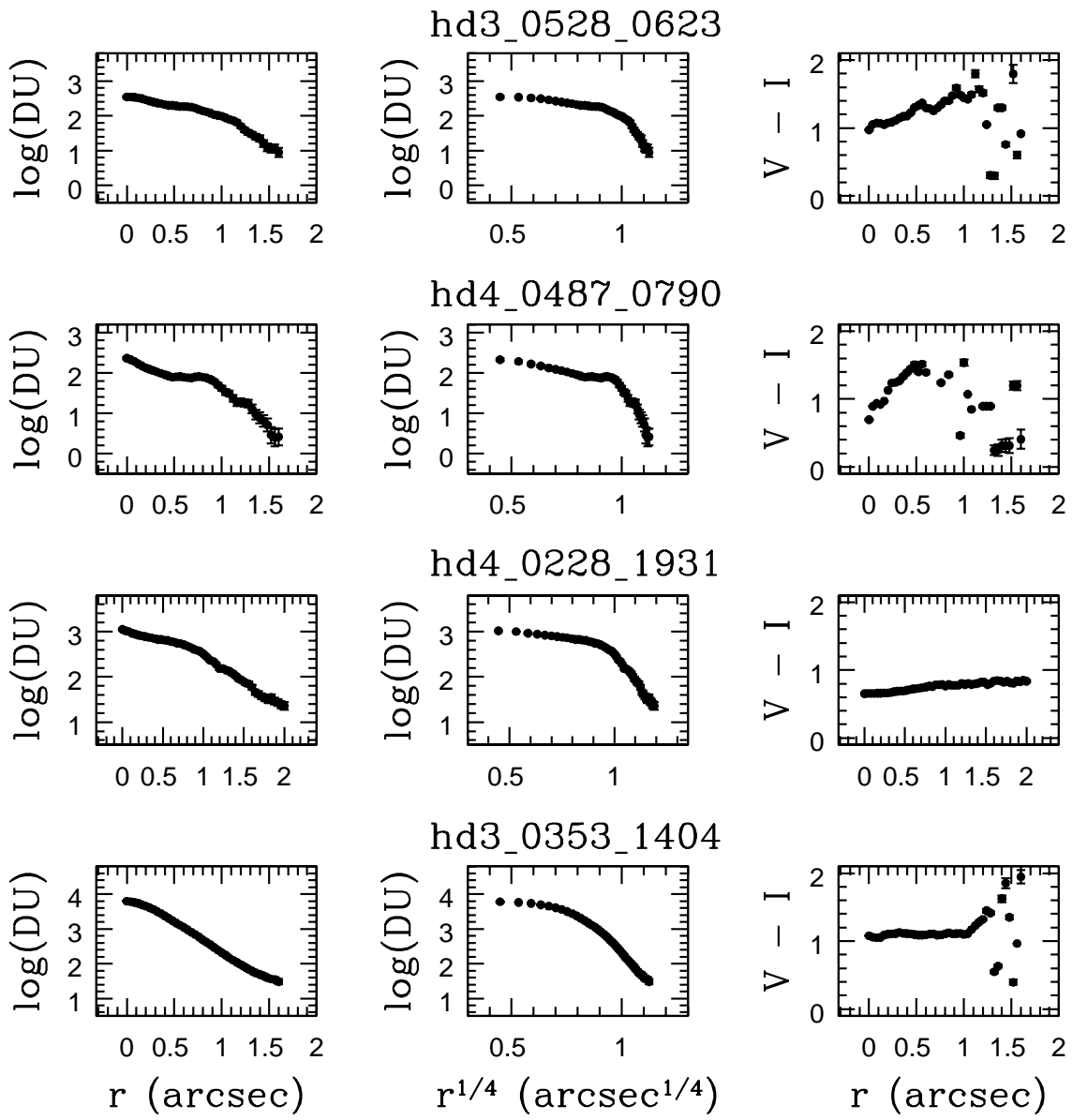
hd4\_1815\_0519



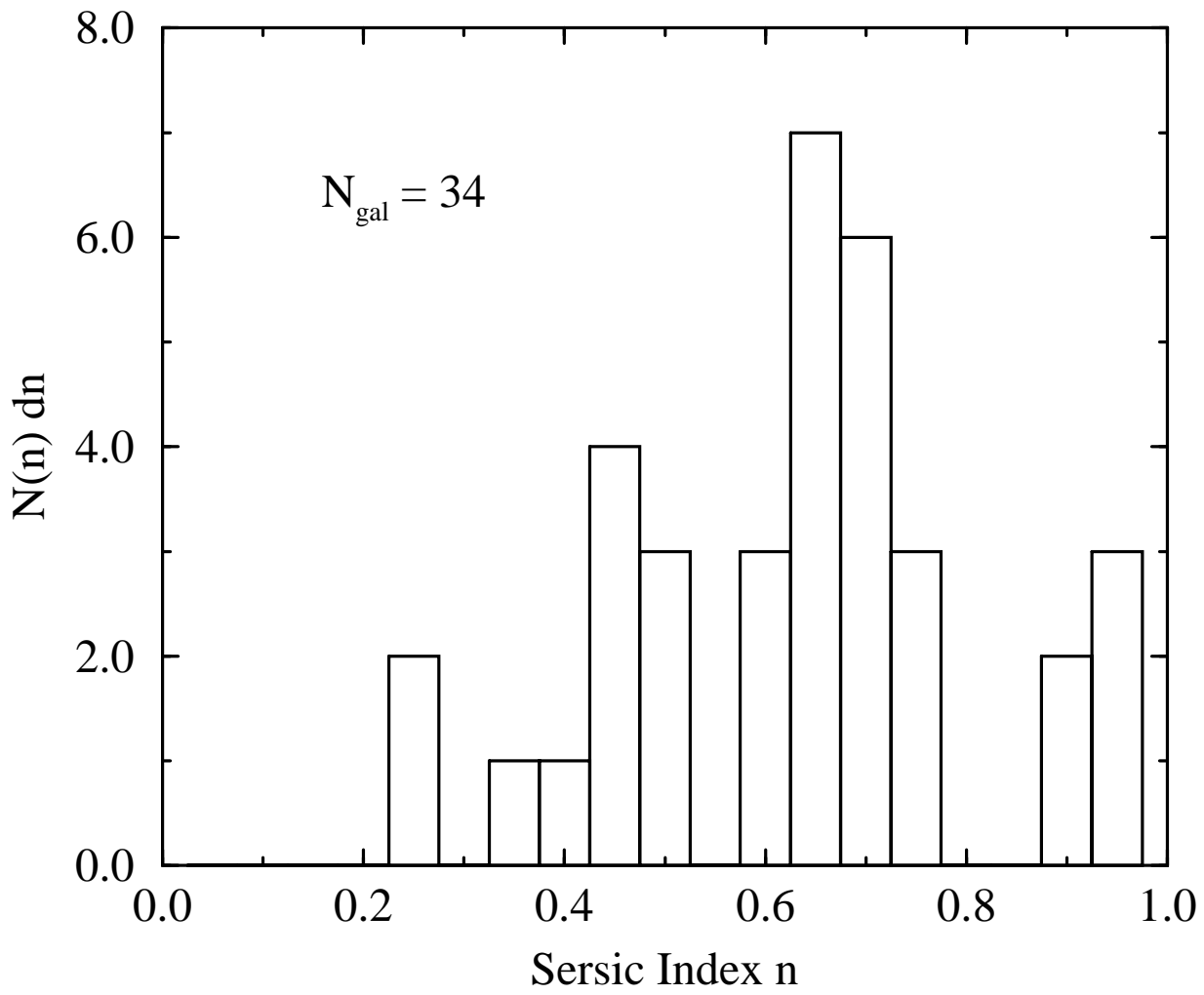
hd4\_0894\_1692

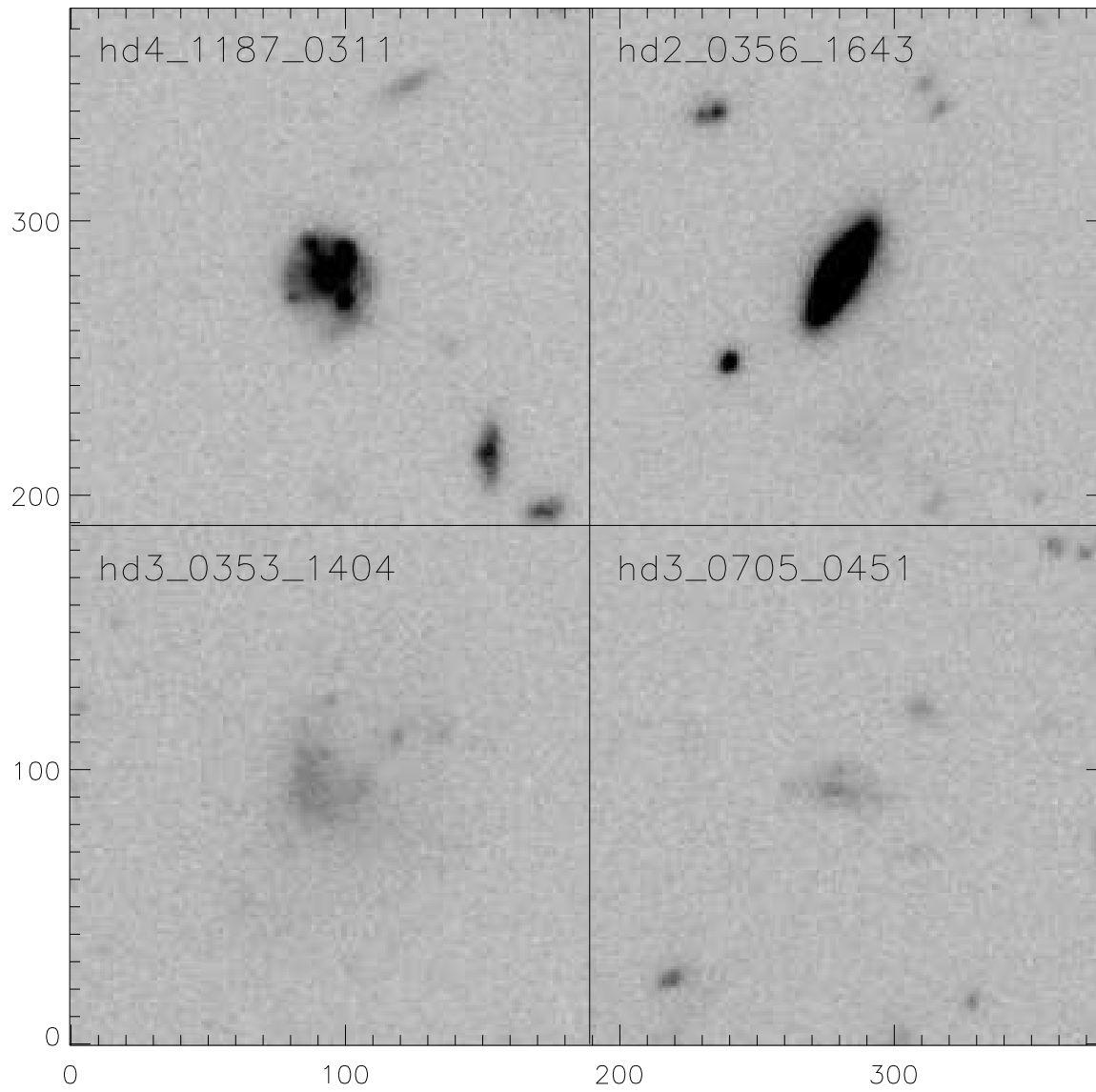


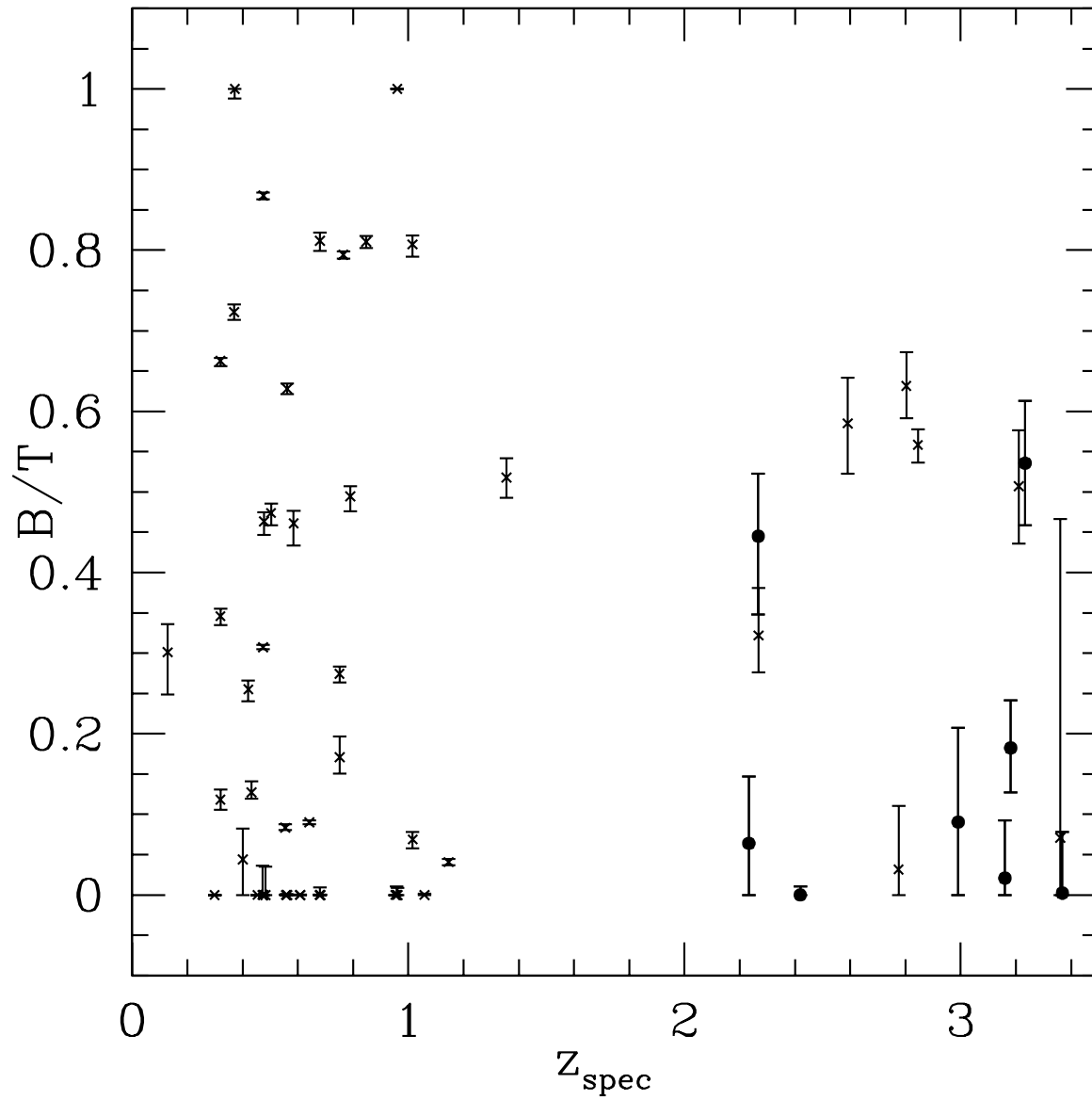












This figure "marleau98\_fig1.jpg" is available in "jpg" format from:

<http://arxiv.org/ps/astro-ph/9807223v1>